Transport rates and momentum isotropization of gluon matter in ultrarelativistic heavy-ion collisions

Zhe Xu[1] * and Carsten Greiner [1]

[1] *Institut für Theoretische Physik, Johann Wolfgang Goethe-Universität Frankfurt, Max-von-Laue-Str.1, D-60438 Frankfurt am Main, Germany*

(Dated: March 2007)

Abstract

In order to describe momentum isotropization of gluon matter produced in ultrarelativistic heavy-ion collisions, the transport rate of gluon drift and the transport collision rates of elastic $gg \leftrightarrow gg$ as well as inelastic $gg \leftrightarrow ggg$ pQCD scattering processes are introduced and calculated within the kinetic parton cascade **BAMPS** (short for Boltzmann Approach of MultiParton Scatterings) simulating the space time evolution of partons. It is demonstrated that the inverse of the introduced total transport rate gives the correct timescale of momentum isotropization. The contributions of the various scattering processes to momentum isotropization can be well separately quantified according to their transport collision rates. The determinant effect of the distribution of collision angle on momentum deflection is rather implicitly, but correctly involved in the transport collision rate than in the transport cross section. Based on the calculated transport collision rates from the BAMPS for a central Au+Au collision at RHIC energy, we show that the pQCD $gg \leftrightarrow ggg$ Bremsstrahlung processes are a factor of 5 more efficient for momentum isotropization compared to the elastic scatterings. The large efficiency of the Bremsstrahlung stems mainly from the large momentum deflection in the process. In addition, due to the kinematic reason a $2 \rightarrow N$ $(N > 2)$ production process allows more particles to become isotropic in momentum space and thus is more efficient for kinetic equilibration than its back reaction as well as the elastic scattering. We also show that the relaxation time in the often employed relaxation time approximation is strongly momentum dependent and thus cannot serve as a global quantity describing kinetic equilibration.

PACS numbers: 25.75.-q, 12.38.Mh, 05.60.-k, 24.10.Lx

* E-mail: xu@th.physik.uni-frankfurt.de

I. INTRODUCTION AND MOTIVATION

It is speculated that the Quark Gluon Plasma (QGP) created in Au+Au collisions at RHIC is a strongly coupled liquid [1]. This strong coupling, or strong interaction, makes the QGP to a fluid with very small viscosity. However, how the strong coupling comes about and how strong the coupling must be, in order to generate a quasi-ideal fluid, are open and fundamental questions. The necessary condition for the onset of a perfect hydrodynamical expansion is the achievement of local kinetic equilibrium. While the initial condition for the quarks and gluons produced at RHIC is far from thermal equilibrium, kinetic equilibration should occur on a short timescale in order that a large elliptic flow v_2 can be subsequently built up [2, 3, 4]. In the following we restrict ourselves to understand the strong coupling and thermalization as a consequence of frequent collisions among gluons on a semi-classical level. To study the issue quantitatively we have recently developed a new on-shell parton cascade **BAMPS** (short for Boltzmann Approach of MultiParton Scatterings) [5] which is a microscopical, relativistic transport model solving the Boltzmann equation of partons produced in ultrarelativistic heavy-ion collisions. Interactions included in the BAMPS are elastic $gg \leftrightarrow gg$ as well as inelastic $gg \leftrightarrow ggg$ pQCD Bremsstrahlung processes. We have shown that although the total cross section of the pQCD scatterings is only a few mb, it is enough to drive the system towards full themal equilibrium [5] and also to generate sufficiently large elliptic flow v_2 [6]. The question to be addressed is how to understand the numerically observed fast equilibration of gluons in theoretical terms. This is the prior motivation of our present investigation.

In kinetic theory there are two competitive processes which affect kinetic equilibration. The first one is the free streaming of particles between two subsequent collisions. For an expanding system the free streaming brings the system out of equilibrium. This is especially true in an one-dimensional Bjorken expansion which is probably the case at the early time in an ultrarelativistic heavy-ion collision. The second one are collisions which make the momentum of particles kinetically isotropic and thermal. Here one has to take into account the distributions of collision angles, since large-angle collisions should contribute more to momentum isotropization. Mathematically a *transport cross section* [7, 8], either in the form

$$\sigma^{tr.} = \int d\theta \frac{d\sigma}{d\theta} sin^2\theta \tag{1}$$

or

$$\sigma^{tr.} = \int d\theta \frac{d\sigma}{d\theta}(1 - cos\theta)\,, \tag{2}$$

was introduced as a pertinent quantity measuring the contributions of various collision processes to kinetic equilibration. However, while kinetic equilibration is observed locally in the co-moving frame of a considered piece of the expanding system, the transport cross section is usually calculated in the center-of-mass (CM) frame of individual colliding particles. The changes of momenta after collisions may look quite different in the different frames. Therefore, the intuitive concept of the transport cross section may, in general, not be fully appropriate for characterizing kinetic equilibration.

Another simplified way to characterize kinetic equilibration, which has been widely used, is to calculate or estimate the relaxation time $\tau_{rel.}$ [9, 10, 11, 12, 13, 14, 15]. In the relaxation time approximation the collision term is expressed by $(f_{eq.} - f)/\tau_{rel}$, where $\tau_{rel.}$ is assumed to be momentum independent and then becomes a global quantity charaterizing the timescale of kinetic equilibration. However, one has to verify that the approximation is applicable to the underlying investigation.

In this paper we want to show a mathematically correct way of quantifying the contribution of various different processes to momentum isotropization. The main issue is the to be defined *transport rate*. It is a momentum average according to the particle density $f(x, p)$ which is the solution of the Boltzmann equation within the parton cascade. We will demonstrate that the inverse of the total transport rate gives the global timescale of momentum isotropization. In section II we mention the operation of the employed parton cascade BAMPS and several improvements. The initial condition of gluons, as an input for the parton cascade, is discussed in section III. We show results on thermal equilibration and momentum isotropization of gluons in section IV for a central Au+Au collision at RHIC energy $\sqrt{s} = 200$ GeV. The inclusion of quarks into the parton cascade is straightforward and the results will be presented in another paper. In section V we define the transport rates determining contributions of various processes to momentum isotropization and derive their relations to the standard concept of the transport cross sections. We present in section VI the numerical results on the transport rates. The transport rate of gluon drift is computed and compared with that when assuming Bjorken boost-invariance. In order to show the importance of the Bremsstrahlung processes in thermal equilibration, we carry out, for comparison, simulations with and without these processes. The quantitative difference in

momentum isotropization for both simulations is manifested by the ratio of the total transport rates. The ratio (which turns out to be approximately 6) is used to perform a third type of simulation in which only elastic scatterings, but with artificially enlarged cross sections are included. Although such large cross sections cannot be motivated from a physical point of view, they serve to verify our main finding: the total transport collision rate is the key quantity determining momentum isotropization. The same total transport collision rate leads to the same momentum isotropization, independently on the details of the incorporated collision processes. At the end of section VI we demonstrate that the relaxation time approximation does not really apply to quantify the timescale of kinetic equilibration. A summary of our findings will be given in section VII. In Appendix A detailed expressions for calculating the transport rates are derived.

II. BAMPS AND SETUP

The structure of the parton cascade BAMPS is based on the stochastic interpretation of the transition rate [5, 16, 17, 18]. This interpretation guarantees obeying detailed balance, which is, by contrast, a difficult task when using the geometrical concept of cross section [19], especially for multiple scatterings like $ggg \leftrightarrow gg$. The particular feature of the numerical implementation in the BAMPS is the subdivision of space into small cell units. In each cell transition probabilities of all possible gluon pairs and triplets are separately evaluated for randomly sampling whether a particular scattering (or transition) occurs or not. The smaller the cells, the more locally transitions can be realized. On the other hand, the smaller the cells, the fewer particles will be inside one cell and thus the larger is the statistical fluctuation in the calculated transition rate. In order to achieve enough pairs and triplets of gluons in a cell, we adopt a test particle technique which amplifies the (pseudo)gluon density by a factor N_{test}. Accordingly the cross sections have to be reduced by the same factor to obtain the same physical mean free path. A detailed implementation and demonstration of the new scheme have been performed in [5]. For calculations carried out in this paper, the transverse length of a cell is set to be a constant, $\Delta x = \Delta y = 0.25$ fm, and the longitudinal length Δz is halved compared to the setup in [5]. For instance for the cell in the collision center $\Delta z \approx 0.1t$, where t is the running time of the gluon evolution. The number of N_{test} is set to be 280 which ensures that there are, on the average, 15 test particles per each cell.

The differential cross section for the pQCD elastic scatterings of gluons is given by

$$\frac{d\sigma^{gg\to gg}}{dq_\perp^2} = \frac{9\pi\alpha_s^2}{(q_\perp^2 + m_D^2)^2}\,. \tag{3}$$

The three-body gluonic interactions are described by the effective matrix element [13, 20, 21]

$$|\mathcal{M}_{gg\to ggg}|^2 = \frac{9g^4}{2}\frac{s^2}{(\mathbf{q}_\perp^2 + m_D^2)^2}\,\frac{12g^2\mathbf{q}_\perp^2}{\mathbf{k}_\perp^2[(\mathbf{k}_\perp - \mathbf{q}_\perp)^2 + m_D^2]}\,\Theta(k_\perp\Lambda_g - \cosh y)\,, \tag{4}$$

where $g^2 = 4\pi\alpha_s$. The coupling α_s is set to be a constant of 0.3 (in contrast to the running coupling involved in [5]) . $\mathbf{q}_\perp$ and $\mathbf{k}_\perp$ denote, respectively, the perpendicular component of the momentum transfer and that of the momentum of the radiated gluon in the center-of-mass frame of the collision. We regularize the infrared divergences by introducing the Debye screening mass m_D

$$m_D^2 = 16\pi\alpha_s N_c \int \frac{d^3p}{(2\pi)^3}\frac{1}{p}\,f_g \tag{5}$$

($N_c = 3$), which is calculated locally over the current gluon density obtained from the simulation. The suppression of the radiation of soft gluons due to the Landau-Pomeranchuk-Migdal (LPM) effect [5, 13, 21], which is denoted via the step function in (4), is modeled by the consideration that the time of the emission, $\sim \frac{1}{k_\perp}\cosh y$, should be smaller than the time interval between two scatterings or equivalently the gluon mean free path Λ_g. This leads to a lower cutoff for $k_\perp$ and to a decrease of the total cross section or the transition probability.

Comparing to the default setup in [5] further improvements are made. In order to calculate the screening mass m_D in a local region more accurately, we make use of the spherical symmetry in central collisions and divide transverse plan in each Δz-bin into rings: from center to outer the first ring has a region of $0 < x_T < 1.5$ fm (x_T being the transverse radius), and the next rings have a width of 1 fm in transverse radius. The rings are regarded as local regions where the screening mass will be evaluated.

Second, in [5] the local collision rates of all interaction channels, the sum of which is the inverse of the mean free path applied to model the LPM effect, were evaluated in individual cells. This leads to large fluctuations in the mean free path in those cells with small number of (test) particles. In order to reduce these fluctuations, we take the averaged value of the collision rates over all the cells within individual rings. In addition, transverse velocities of rings are taken into account for calculating the collision rates in the co-moving frame.

Moreover, we assume that if the energy density which is calculated locally in the co-moving frame decreases under 1 GeV/fm^3, particles in that region do not interact any more and propagate freely. At this stage a hadronization procedure should be applied, which is one of the future developments.

For our further discussions we concentrate on the central region of the full reaction, which is defined as a cylinder with $0 < x_T < 1.5$ fm and $-0.2 < \eta < 0.2$, where η denotes the space-time rapidity $\eta = \frac{1}{2} \ln \frac{t+z}{t-z}$. The longitudinal extension of the cylinder is thus $\Delta z = 2t \tanh(0.2) \approx 0.4t$. The parameters for bounding the cylinder are chosen by the balance of having a small and local region on the one hand and being able to achieve sufficient statistics on the other hand. Results which will be shown below are obtained in this region by sufficient ensemble averaging.

III. INITIAL CONDITION

The initial gluons are taken as an ensemble of minijets with transverse momentum being greater than 1.4 GeV, which are produced via semihard nucleon-nucleon collisions [22]. Details of the distribution of the initial gluons in space and time can be found in [5]. Using Glauber-geometry and assuming independent binary nucleon-nucleon collisions, the gluon number is initially about 700 per momentum rapidity. These gluons take about 60% of the total energy entered in a central Au+Au collision. The lower momentum cut-off is taken as a parameter to fit the experimentally measured final transverse energy at midrapidity (see Fig. 9).

For simplicity one may assume that the two gold nuclei are extremely Lorentz contracted with zero width. If assuming further that on-shell gluons are immediately formed (without any formation time) at the same time when the corresponding nucleon-nucleon collision occurs, all initial gluons are positioned at $z = 0$ fm at $t = 0$ fm/c. Subsequent evolution of a free streaming would immediately order the gluons with the momentum rapidity y to a spatial slice with the space-time rapidity η being equal to y. In the co-moving frame of each spatial slice gluon momentum has only a transverse component, and its distribution is thus highly anisotropic.

At RHIC energy each of the colliding gold nuclei does have a small but not vanishing longitudinal extension of 0.2 fm. Therefore gluons are mostly produced at $z = 0$ fm (or

$\eta = 0$) at $t = 0.1$ fm/c when two nuclei overlap fully. Note that $t = 0$ fm/c is set when two nuclei are just in touch. Compared with the simplified case mentioned above there is thus a significant smearing in the $\eta - y$ correlation of gluons for times $t \leq 0.2$ fm/c. For instance, gluons with $y \neq 0$ will also appear in the central slice with $\eta = 0$ for a while. How fast the smearing will disappear is demonstrated in Fig. 1, where spectra of transverse and longitudinal momentum of gluons are depicted during an initial free streaming in absence of secondary collisions. The spectra are obtained in the central region ($0 < x_T < 1.5$ fm and

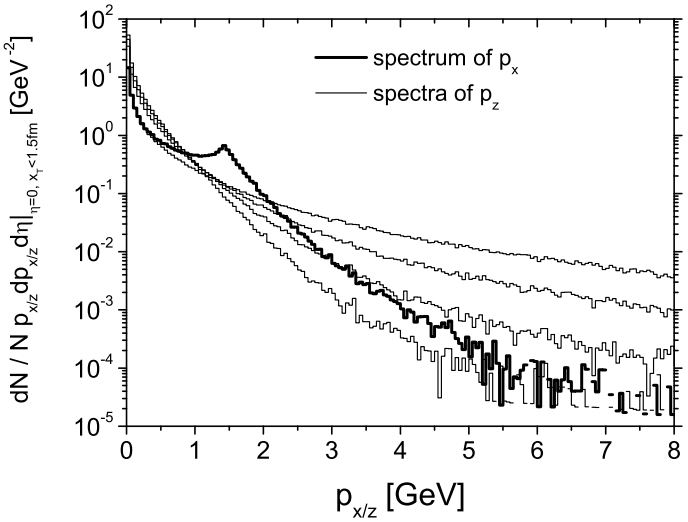

FIG. 1: Spectra of transverse and longitudinal momentum of gluons during an initial free streaming. The thick histogram shows the distribution of $|p_x|$ at a time of 0.1 fm/c, while the thin histograms show the distributions of $|p_z|$ at times of 0.1, 0.2, 0.22 and 0.24 fm/c, respectively from uppermost to lowest one. The results are obtained from the central region.

$-0.2 < \eta < 0.2$). We see that the spectrum of $|p_z|$ changes quite drastically after 0.2 fm/c at which the overlapping of two gold nuclei comes to the end and the production of minijets is completed. The free streaming of high $|p_z|$ gluons away from the central region leads to a strong and continuing suppression in the spectrum of $|p_z|$. The according changes at low transverse momentum in the spectrum of $|p_x|$ are, however, tiny compared with the absolute value at low $|p_x|$. At high $|p_x|$ one does not recognize any changes in time, because for large nuclei there is no transverse expansion at the beginning. Therefore, in Fig. 1 the spectrum of $|p_x|$ is only depicted at one time point $t = 0.1$ fm/c. We note that the suppression at large $|p_z|$ will slow down and stop at a later time when all particles with high p_z (or with

high $y > \eta_b = 0.2$) have left a small, but finite rapidity window ($\eta : [-\eta_b : \eta_b]$). There are then only particles with lower rapidity y sitting in the central region. For instance, the time which a gluon needs to go out of the central region is $\Delta t = t_0 \tanh\eta_b/(\tanh y - \tanh\eta_b)$ when the gluon is produced at $z_0 = 0$ fm at t_0. We see that the larger the momentum rapidity y, the smaller is Δt. For a gluon with $y = 1$ and $t_0 = 0.1$ fm/c it takes $\Delta t = 0.035$ fm/c to go out of the central region.

Comparing the particle spectrum of $|p_z|$ with that of $|p_x|$, the momentum distribution is, strictly speaking, at no time isotropic during the initial free streaming. The characteristic hump in the spectrum of $|p_x|$ at 1.4 GeV comes from the requirement that the transverse momentum of the original minijets should be greater than 1.4 GeV. Choosing other initial conditions like in HIJING [23] or Color Glass Condensate [24] would change the shape of the initial momentum distribution. However, even though the momentum distribution might be isotropic at a certain time during the continuing suppression of high $|p_z|$ gluons, the further suppression would bring the momentum distribution out of isotropy within a very short time of ~ 0.1 fm/c. Therefore, we can conclude that free streaming leads to $\eta \approx y$ irrespective of what the initial $\eta - y$ correlation is. The momentum distribution of gluons after a short-time free streaming is in general neither thermal nor isotropic.

For the calculations carried out in this paper we introduce an additional *formation time* [5] for every minijets, $\Delta t_f = \cosh y \Delta\tau_f \approx \cosh y \cdot 1/p_T$, which models the prior off-shell propagation of the gluons to be freed in the individual nucleon-nucleon collisions. $\cosh y$ denotes the Lorentz factor. Within the time span Δt_f, we assume that the still virtual gluon does not interact and moves freely with the speed of light. Gluons with large $|p_z|$ have large Lorentz factor and thus have a large formation time. Although most of these gluons are produced in the central region, they are definitely out of the central region when they materialize as on-shell partons, because of the assumed off-shell propagation. Since we count particles only if they are on-shell (i.e. being interactive), the momentum distribution of initial (at 0.2 fm/c) gluons differs from that shown in Fig. 1, but is nearly the same as that at 0.24 fm/c, which is not isotropic. Choosing such an initial condition and performing a simulation including the pQCD Bremsstrahlung processes, we obtain dE_T/dy about 640 GeV at midrapidity at a final time of 5 fm/c, at which the energy density of gluons decreases to the critical value of 1 GeV/fm^3. That value of dE_T/dy at $y = 0$ obtained from the simulation is comparable with that from the experimental measurements at RHIC [25] (see Fig. 9).

IV. MOMENTUM ISOTROPIZATION AND KINETIC EQUILIBRATION

Kinetic equilibration is a process in which the momentum of particles is getting isotropic and thermal, possessing an exponential shape in its distribution. Momentum isotropization is part of kinetic equilibration and will be completed at an earlier timescale than the achievement of full kinetic equilibrium [26, 27, 28, 29]. (Strictly speaking, a full kinetic equilibrium can only be achieved for a static, but not for an expanding system.) In this paper we concentrate on the contribution of collision processes to momentum isotropization and kinetic equilibration of gluon matter in an ultrarelativistic heavy-ion collision.

As demonstrated in section III, the initial free streaming (or the off-shell propagation) of gluons with high momentum rapidity y makes the momentum distribution anisotropic, even it momentarily looks isotropic. The initial situation in the central region is that most gluons are moving in the transverse direction. Secondary collision processes will gradually bring them more or less to the longitudinal direction, which gives a positive contribution to momentum isotropization. On the other hand, whenever a gluon is turned in the longitudinal direction, its momentum rapidity becomes larger and it tends to drift out of the central region. This gives a negative contribution to momentum isotropization in the local region. Although gluons with the same (irrespective of $\pm$ sign) momentum rapidity are also drifting from the neighboring slices into the central slice, this cannot completely compensate the loss in the central region. The reason is that thermalization occurs earlier in the central slice than in the outwards regions corresponding to Bjorken's picture of boost-invariance in the space-time evolution of the parton system [30]. In the transverse direction, however, there is no transverse flow at the beginning of the expansion. Therefore, no net drift of gluons occurs in the transverse direction. The different drifting of gluons in the longitudinal and transverse direction leads to a situation that the net effect of the drift has a negative contribution to momentum isotropization, and that the stronger the momentum isotropization, the larger is the negative contribution of the particle drift. At late times when three-dimensional expansion takes place there is also net particle drift in the transverse direction. The contribution of the particle drift to momentum isotropization becomes then less negative.

In this section we first demonstrate momentum isotropization and kinetic equilibration of gluons in a central Au+Au collision at RHIC energy. The various contributions of collisions and drift to momentum isotropization will be analysed in the next section in detail. Figure

2 depicts distributions of the transverse and longitudinal momentum of gluons in the central region at four different times during the gluon evolution. The results shown are obtained

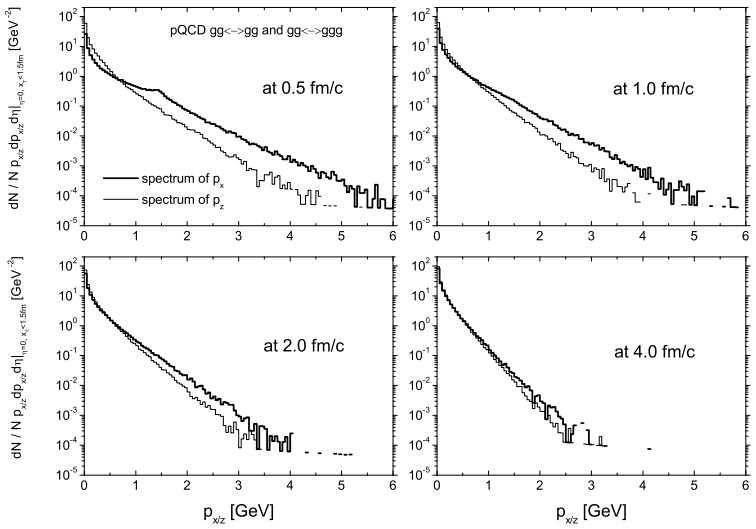

FIG. 2: Spectrum of the transverse (thick histograms) and longitudinal (thin histograms) momentum of gluons in the central region at different times during the gluon evolution. Results are obtained from the simulation including both elastic and inelastic pQCD scattering processes.

from the simulation including both elastic and inelastic pQCD based scattering processes. We first see that the momentum distribution is continuously getting isotropic and thermal in progressing time. We note that due to the expansion no full thermal equilibrium can be achieved if the collision rate is finite. A certain mismatch in p_Z and p_X has to prevail because of the counterplay between expansion and collisions.

Secondly we observe from Fig. 2 that the distribution has already possessed an exponential shape before it becomes isotropic. One can hardly distinguish the timescale at which the gluon momentum becomes isotropic from that at which the system becomes fully thermal. It seems that when collisions bring the momentum of particles close to isotropic, the momentum distribution is also already close to thermal. In general, momentum isotropization happens on a shorter timescale than kinetic equilibration. The difference in the timescales of both dynamical processes depends on the initial condition of gluons.

We also realize that kinetic equilibration for the softer gluons is earlier completed than that for the harder gluons. This is clear for elastic $gg \leftrightarrow gg$ scattering processes, since the momentum transfer in all collisions is typically the screening mass m_D. Therefore, the

hard gluons cannot be deflected so strongly as the soft gluons. On the other hand, in the inelastic pQCD $gg \leftrightarrow ggg$ collisions, which we will soon realize to be the dominant processes in kinetic equilibration, the momentum degradation for the soft and hard gluons is not much different due to the production or absorbtion of one additional gluon. Averaging the different timescales of approaching kinetic equilibrium for the soft and hard gluons, the momentum distribution becomes *isotropic and thermal at* $1-2$ *fm/c*. Furthermore we clearly see that the distributions become more and more steeper, which indicates the ongoing cooling of the system related to a quasi hydrodynamical behavior due to the subsequent work done by the expanding system.

In order to understand the role of the inclusion of the inelastic pQCD $gg \leftrightarrow ggg$ processes in kinetic equilibration, we also carry out calculations in which gluons interact only via elastic scatterings. The initial condition is the same as that for the simulation including the inelastic collisions. The results are shown in Fig. 3 which is organized in the same way as in Fig. 2. The difference in the results depicted in both figures is immediately seen. The

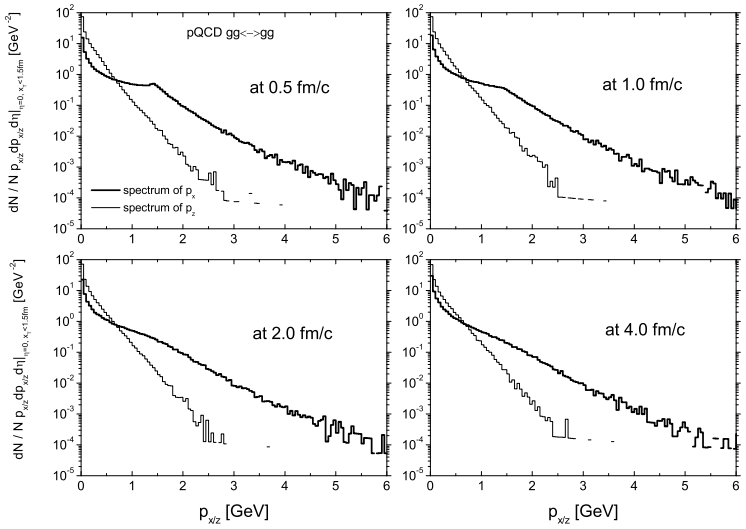

FIG. 3: Spectrum of the transverse (thick histograms) and longitudinal (thin histograms) momentum of gluons in the central region at different times during the gluon evolution. Results are obtained from the simulation including only elastic pQCD scattering processes.

spectra in Fig. 3 only show a small change during the whole evolution and are still highly anisotropic and nonthermal at the late time 4 fm/c. The evolution resembles that of a free streaming.

There is a dramatic difference in kinetic equilibration whether the pQCD Bremsstralung processes and their back reactions are taken into account, or not. It shows that the pQCD Bremsstrahlung processes and their back reactions play an essential role in early thermalization of gluons in heavy-ion collisions at RHIC. They are much more efficient for momentum isotropization than the elastic collisions. On the other hand, as seen in Fig. 4, the pQCD cross section of the $gg \to ggg$ processes including the LPM suppression (dashed curve) is *smaller* than that of the elastic scatterings (solid curve) and much smaller than the cross section obtained in the simulation with only elastic scattering processes (dotted curve). Although particle production in inelastic processes can enhance the number of collision cen-

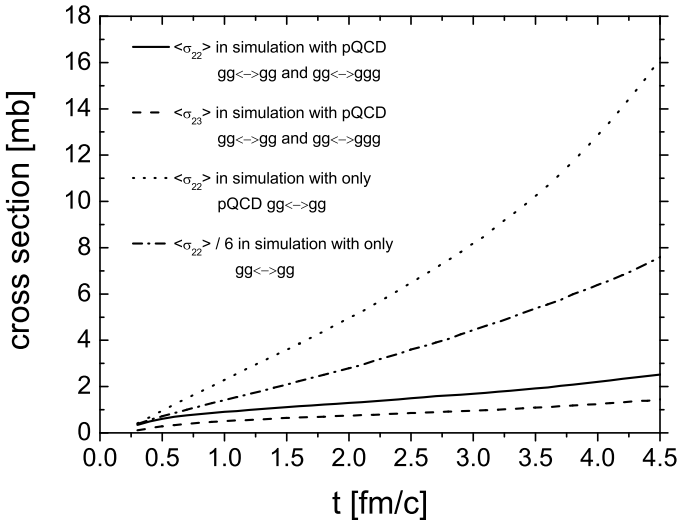

FIG. 4: Time evolution of pQCD cross sections. The cross sections are averaged over collision pairs in the central region. The solid and dashed curve show, respectively, the pQCD cross section for $gg \to gg$ and $gg \to ggg$ collisions in the simulation with both elastic and inelastic scattering processes. The dotted curve gives the cross section of $gg \to gg$ collisions in the simulation including only elastic pQCD scattering processes, while the dash-dotted curve indicates the cross section (*divided by* 6) of $gg \to gg$ collisions in the simulation including only elastic scattering processes with artificially large cross sections.

ters, and thus effectively shorten the mean free path of particles, chemical equilibration will balance the production by the annihilation of particles to avoid oversaturation. The fact that the cross section of the pQCD Bremsstrahlung process is small, but its efficiency for kinetic equilibration is large, demonstrates that cross sections or collision rates cannot

manifest the contributions of various processes to kinetic equilibration. At least one has to take the distribution of the collision angle into account. How to find and define the correct quantity is one of the main purpose of this paper.

From Fig. 4 one recognizes the big difference in the total cross sections of the elastic scatterings when comparing the results from the different simulations, the solid curve versus the dotted curve. Since

$$< \sigma_{gg\to gg} > \sim \frac{1}{m_D^2 \ < 1 + 4m_D^2/s >}\,, \tag{6}$$

the large difference in the cross sections comes from the different developments of the screening mass m_D in the different simulations. The screening mass is calculated dynamically according to (5) and thus is approximately proportional to $\sqrt{n/ < p >} = n/\sqrt{\epsilon}$, where n and ϵ are, respectively, the number and energy density of gluons. We consider two extreme cases of expansion beginning with an initial condition which possesses the longitudinal boost invariance. One is the free streaming. In this case n as well as ϵ decreases as $1/\tau$, where $\tau = \sqrt{t^2 - z^2}$ is the proper time. Thus the screening mass decreases as $1/\tau^{1/2}$. In the case of an one-dimensional ideal hydrodynamical expansion n decreases as $1/\tau$, while ϵ decreases as $1/\tau^{4/3}$. Therefore, m_D decreases as $1/\tau^{1/3}$. In a viscous hydrodynamical expansion the decrease of m_D in time is in between of the two cases. More complicated is the time dependence of the screening mass in a real expansion beginning with a nonthermal state and undergoing thermalization. While kinetic equilibration relaxes the density distribution of gluons to the thermal shape, which affects the calculation in the screening mass (5), chemical equilibration which is not taken into account in the above analyses will enhance or reduce the gluon number, which in turn enhances or reduces m_D. Figure 5 shows the time evolution of the screening mass in different simulations. The results are obtained in the central region where $t \approx \tau$. All the curves in Fig. 5 decrease in time. We see different evolutions in different simulations: In the simulation including both elastic and inelastic pQCD scatterings (solid curve) m_D decreases more slowly than $1/t^{1/3}$ due to gluon production in the course of chemical equilibration. In the simulation with only elastic pQCD collisions the decrease of the screening mass (dotted curve) is slightly stronger than $1/t^{1/2}$, which indicates again that the expansion of gluons in this simulation resembles that of a free streaming. The third simulation including only elastic scatterings with artificially large cross sections has a same kinetic equilibration as that in the simulation including both elastic and inelastic pQCD

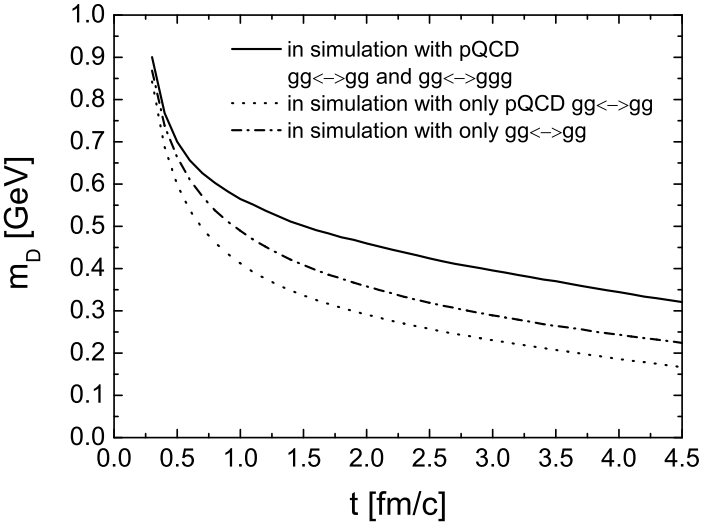

FIG. 5: Time evolution of screening mass. The solid, dotted and dash-dotted curve display, respectively, the results obtained from the simulation with both pQCD elastic and inelastic collisions, with only pQCD elastic collisions and with only elastic collisions using large cross sections.

collisions (see later in this section and see also section VI). Since elastic collisions conserve the particle number and no particle production and annihilation occur to realize chemical equilibration, the screening mass decreases between $1/t^{1/2}$ and $1/t^{1/3}$.

In principle, the timescale of kinetic equilibration of gluons can be quantitatively achieved by studing the entropy production. Since the entropy can be hardly extracted from any microscopic cascade, we concentrate on momentum isotropization of gluons. For the present example of gluon evolution choosing the minijets production as the initial condition, we have already seen that the timescales of momentum isotropization and kinetic equilibration are almost the same (see Fig. 2).

To quantify momentum isotropization, it is convenient to take a certain moment of the momentum distribution. For instance, we define $< p_Z^2/E^2 >$ as the momentum isotropy to describe momentum isotropization. Later we will briefly discuss the consequences on the obtained results if the momentum isotropy is defined by $< |p_Z|/E >$, in order to see how sensitive the results are to different descriptions of momentum isotropization. In Fig. 6 the time evolution of the momentum isotropy is depicted. The average is taken over all gluons in the central region. From Fig. 6 we see that while the momentum isotropy relaxes to the value at equilibrium, 1/3, in the simulation including the inelastic processes, the

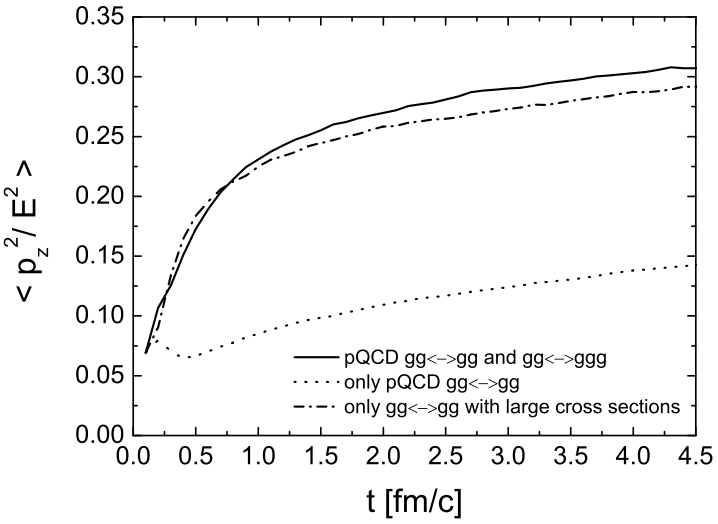

FIG. 6: Time evolution of the momentum isotropy. Results are obtained, respectively, from the simulation including both elastic and inelastic pQCD scattering processes (solid curve), including only elastic pQCD scattering processes (dotted curve) and including only elastic scattering processes with artificially large cross sections (dash-dotted curve).

momentum isotropy is still far from the equilibrium value at the latest time 4.5 fm/c in the simulation with only elastic pQCD scatterings. These results agree with the time evolution of the momentum spectra shown in Figs. 2 and 3. The dash-dotted curve in Fig. 6 depicts the time evolution of the momentum isotropy in the simulation with only elastic collisions, but artificially large cross sections, and is almost the same as the solid curve presenting the result in the simulation including the pQCD Bremsstrahlung processes. This indicates basically the same kinetic equilibration in the two simulations. The details about the setup in the third simulation will be explained later in section VI.

We fit the time evolution of the momentum isotropy using the relaxation formula

$$F(t) = \frac{1}{3} + \left(< \frac{p_Z^2}{E^2} > (t_0) - \frac{1}{3} \right) \exp\left(-\frac{t - t_0}{\theta_{rel.}(t_0)}\right). \tag{7}$$

The momentum isotropy is labeled now by $Q := < p_Z^2/E^2 >$. $F(t)$ is strictly only equal to $Q(t)$ at $t = t_0$. For fixed t_0 the relaxation time $\theta_{rel.}$ is a constant with respect to t. Such a fit can be done at every time point t_0. Using $\theta_{rel.} = 0.9$ fm/c at $t_0 = 0.3$ fm/c $F(t)$ fits perfectly the solid curve in Fig. 6 up to 1.0 fm/c and using $\theta_{rel.} = 2.4$ fm/c at $t_0 = 1.2$ fm/c $F(t)$ fits the rest. We find that an isotropic state is achieved at about 1.0 fm/c in the simulation including both elastic and inelastic pQCD scattering processes. This timescale is

consistent with that extracted from the momentum distribution (compare with Fig. 2). We conclude that within our parton cascade description, early thermalization happens as fast as 1 fm/c for the initially nonequilibrium gluon matter at RHIC.

We also see that the relaxation time $\theta_{rel.}$ is generally time dependent. The two values of $\theta_{rel.}$ are obtained by fitting. Actually $\theta_{rel.}$ can be calculated exactly, since in order to make a local fit one should request that the time derivatives of $F(t)$ and $Q(t)$ are equal at $t = t_0$. This leads to

$$\dot{Q}(t)\Big|_{t=t_0} = \dot{F}(t)\Big|_{t=t_0} = -(Q(t_0) - Q_{eq.})\,\frac{1}{\theta_{rel.}(t_0)} \tag{8}$$

with $Q_{eq.} = 1/3$. Changing t_0 to t gives

$$\frac{\dot{Q}(t)}{Q_{eq.} - Q(t)} = \frac{1}{\theta_{rel.}(t)}. \tag{9}$$

Equation (9) expresses the relaxation rate $1/\theta_{rel.}$ of the momentum isotropy as a function of time. It serves as the fundamental quantity for our further investigation. In the next section we will analytically separate this relaxation rate into different terms corresponding particle drift and various scattering processes, and we will derive the so-called *transport rate* which *precisely* quantifies the contribution of a certain process to momentum isotropization.

V. TRANSPORT RATE

To introduce the momentum isotropy at a certain space point $\vec{\xi}$ one has to go to its co-moving frame. Suppose that x and p are, respectively, the four-vektor of coordinate and momentum of particles in the co-moving frame of $\vec{\xi}$, the momentum isotropy is defined by

$$Q(t) := < \frac{p_Z^2}{E^2} > \Big|_{\vec{x}=0} = \frac{1}{n}\int \frac{d^3p}{(2\pi)^3}\frac{p_Z^2}{E^2}\ f(\vec{x},t,p)|_{\vec{x}=0}\ , \tag{10}$$

where

$$n(t) = \int \frac{d^3p}{(2\pi)^3}\ f(\vec{x},t,p)|_{\vec{x}=0} \tag{11}$$

is the local number density. In the practice the momentum isotropy is evaluated within a small volume element which is small compared with the volume of the expanding system, but is so large that it still contains a great number of particles. We choose the central region with the boundary $x_T < r_B = 1.5$ fm, $|\eta| < \eta_b = 0.2$ as such a volume element. Correspondingly one has to make changes in (10) and (11). Detaied expressions are derived

explicitly in Appendix A. In the following we consider, for simplicity, the case in the limit $r_b \to 0$ and $\eta_b \to 0$. The definitions (10) and (11) are correct expressions in this limit.

Taking the derivative of $Q(t)$ in time gives

$$\dot{Q}(t) = \frac{1}{n}\int \frac{d^3p}{(2\pi)^3}\frac{p_Z^2}{E^2}\left.\frac{\partial f}{\partial t}\right|_{\vec{x}=0} - Q(t)\frac{1}{n}\int \frac{d^3p}{(2\pi)^3}\left.\frac{\partial f}{\partial t}\right|_{\vec{x}=0} . \tag{12}$$

We replace $\partial f/\partial t$ in (12) by

$$\frac{\partial f}{\partial t} = -\frac{\vec{p}}{E}\cdot\vec{\nabla} f + C_{22} + C_{23} + C_{32} \tag{13}$$

according to the Boltzmann equation. C_{22}, C_{23} and C_{32} denote, respectively, the collision term corresponding to $gg \to gg$, $gg \to ggg$ and $ggg \to gg$ processes. It is obvious that the contribution of the various processes to $\dot{Q}(t)$ is additive. We rewrite Eq. (12) to

$$\dot{Q}(t) = W_{drift}(t) + W_{22}(t) + W_{23}(t) + W_{32}(t)\,, \tag{14}$$

where W_{drift}, W_{22}, W_{23} and W_{32} correspond to particle drift, $gg \to gg$, $gg \to ggg$ and $ggg \to gg$ collision processes respectively. According to (9) we then obtain

$$\frac{1}{\theta_{rel.}(t)} = R^{tr.}_{drift}(t) + R^{tr.}_{22}(t) + R^{tr.}_{23}(t) + R^{tr.}_{32}(t)\,, \tag{15}$$

where we define

$$R^{tr.}_i(t) := \frac{W_i(t)}{Q_{eq.} - Q(t)} \tag{16}$$

with $i = drift$, 22, 23 and 32. One sees that the relaxation rate of momentum isotropization, $1/\theta_{rel.}$, is separated into additive parts corresponding to particle drift and collision processes. $R^{tr.}_{drift}$ is called the *transport rate of particle drift*, while $R^{tr.}_{22}$, $R^{tr.}_{23}$ and $R^{tr.}_{32}$ stand for the *transport collision rates* of the respective interactions. The extension to more than three-body processes is straightforward since the collision term is additive. We note that the mathematical formula of $R^{tr.}_i$ (shown below) depends on which momentum isotropy we are looking at. If one defines $< |p_Z|/E >$ as the momentum isotropy for instance, the form of $R^{tr.}_i$ will alter accordingly by overall changing p_Z^2/E^2 to $|p_Z|/E$.

We now give the detailed expressions of the transport rate of certain processes one by one.

A. $R^{tr.}_{drift}$

Except for a static system the drift term in the Boltzmann equation (13) generally contributes to $\dot{Q}(t)$. W_{drift} is expressed by

$$W_{drift}(t) = \frac{1}{n}\int \frac{d^3p}{(2\pi)^3}\,\frac{\vec{p}}{E}\cdot\vec{\nabla}f\,\left[Q(t)-\frac{p_Z^2}{E^2}\right]. \tag{17}$$

Assuming Bjorken's space-time picture of a central ultrarelativistic heavy-ion collision [30], the relation [9]

$$\frac{\vec{p}}{E}\cdot\vec{\nabla}f \approx \frac{p_Z}{E}\frac{\partial f}{\partial z} = -\frac{p_Z}{t}\frac{\partial f}{\partial p_Z} \tag{18}$$

can be used. Inserting Eq. (18) into (17) and calculating partial integrals give

$$R^{tr.}_{drift}(t) \approx \frac{-2}{[Q_{eq.}-Q(t)]\;t}\left[Q(t) - < \frac{p_Z^4}{E^4} > (t)\right]. \tag{19}$$

The formula (19) shows that $R^{tr.}_{drift}$ is negative, which confirms the qualitative understanding in the previous section. Taking for the moment the approximation $< p_Z^4/E^4 > \approx Q^2$, one can also realize that the larger is Q, the larger is $-R^{tr.}_{drift}$.

B. $R^{tr.}_{22}$

Let us look at W_{22} which is

$$W_{22}(t) = \frac{1}{n}\int \frac{d^3p_1}{(2\pi)^3}\frac{p_{1Z}^2}{E_1^2}\,C_{22}\,. \tag{20}$$

(We have changed p to p_1.) C_{22} has no contribution to the second integral in Eq. (12) due to particle number conservation in elastic collisions. The same is also for the sum of C_{23} and C_{32} at chemical equilibrium. Putting the explicit expression of the collision term via the transition matrix element

$$\begin{aligned} C_{22} \;=\; & \frac{1}{2E_1}\int d\Gamma_2 \frac{1}{2!}\int d\Gamma_1' d\Gamma_2'\, f_1' f_2' |\mathcal{M}_{1'2'\to 12}|^2 (2\pi)^4\delta^{(4)}(p_1'+p_2'-p_1-p_2) \\ & -\frac{1}{2E_1}\int d\Gamma_2\, f_1 f_2 \frac{1}{2!}\int d\Gamma_1' d\Gamma_2'\, |\mathcal{M}_{12\to 1'2'}|^2 (2\pi)^4\delta^{(4)}(p_1+p_2-p_1'-p_2') \end{aligned} \tag{21}$$

($d\Gamma_i = d^3p_i/(2\pi)^3 2E_i$ for short) into Eq. (20) gives two terms which indicate the gain and loss in momentum isotropization.

The loss term can be easily written to

$$\frac{1}{n}\int d\Gamma_1 d\Gamma_2 f_1 f_2 \frac{p_{1Z}^2}{E_1^2}\,2s\,\sigma_{22} = n < v_{rel}\frac{p_{1Z}^2}{E_1^2}\,\sigma_{22} >_2\,, \tag{22}$$

where

$$\sigma_{22} := \frac{1}{2s}\frac{1}{2!}\int d\Gamma_1^{'} d\Gamma_2^{'} \left|\mathcal{M}_{12\to 1'2'}\right|^2 (2\pi)^4 \delta^{(4)}(p_1 + p_2 - p_1^{'} - p_2^{'}) \tag{23}$$

is the total cross section, s is the invariant mass of the colliding system and $v_{rel} = s/2E_1E_2$ is the relative velocity. $<>_2$ symbolizes an ensemble average over incoming particle pairs. In the BAMPS simulations $f(x,p) \approx \sum_i \delta^{(3)}(\vec{x} - \vec{x}_i(t))\delta^{(3)}(\vec{p} - \vec{p}_i)$ and we can approximately evaluate the averages $<>_2$ in local cells by running over all particle pairs in the cells. Each cell has a small volume to keep the locality of collisions, and has sufficient number of (test) particles as well to achieve high statistics.

The gain term of W_{22} can analogously be expressed by $n < v_{rel}\tilde{\sigma}_{22} >_2$ with

$$\tilde{\sigma}_{22} := \frac{1}{2s}\frac{1}{2!}\int d\Gamma_1^{'} d\Gamma_2^{'} \frac{p_{1Z}^{'2}}{E_1^{'2}} \left|\mathcal{M}_{12\to 1'2'}\right|^2 (2\pi)^4 \delta^{(4)}(p_1 + p_2 - p_1^{'} - p_2^{'}) \tag{24}$$

which is an integral over all possible states of outgoing particles. To get the last expression we have exchanged the variables with prime with those without prime in (21). Except $p_{1Z}^{'2}/E_1^{'2}$ other variables and functions in (24) are Lorentz invariant. Particularly $d\Gamma_1^{'} = d\Gamma_1^{'*} = d^3p_1^{'*}/(2\pi)^3 2E_1^{'*} = d\Omega^* dE_1^{'*} E_1^{'*}/2(2\pi)^3$ where $p_1^{'*}$ is the four-momentum of an outgoing particle in the CM frame manifested by p_1 and p_2 of the incoming particles, and Ω^* denotes the solid angle relative to the collision axis in the CM frame. Integration over $d\Gamma_2^{'} = d\Gamma_2^{'*}$ by using the four-dimensional δ function gives

$$\tilde{\sigma}_{22} = \int d\Omega^* \frac{d\sigma_{22}}{d\Omega^*} \frac{p_{1Z}^{'2}}{E_1^{'2}}\,, \tag{25}$$

where $p_{1Z}^{'2}$ and $E_1^{'2}$ are the Lorentz transformed quantities from $p_1^{'*}$ and thus functions of Ω^*, s and $\vec{\beta}$. The latter, $\vec{\beta} = (\vec{p}_1 + \vec{p}_2)/(E_1 + E_2)$, denotes the relative velocity of the CM frame of colliding particles to the lab frame where the momentum isotropy is defined.

We finally obtain

$$R_{22}^{tr.} = \frac{W_{22}}{Q_{eq.} - Q(t)} = \frac{1}{Q_{eq.} - Q(t)} \left(n < v_{rel} \int d\Omega^* \frac{d\sigma_{22}}{d\Omega^*} \frac{p_{1Z}^{'2}}{E_1^{'2}} >_2 - n < v_{rel} \frac{p_{1Z}^2}{E_1^2}\, \sigma_{22} >_2 \right) \tag{26}$$

which expresses the difference of the gain and loss in momentum isotropization. The determinant effect of the distribution of the collision angle on momentum isotropization is implicitly contained. While the collision rate is defined by the standard formula

$$R_{22} = n < v_{rel}\sigma_{22} >_2\,, \tag{27}$$

$R_{22}^{tr.}$ is called the *transport collision rate* of elastic scatterings.

The expression of $R_{22}^{tr.}$ in (26) is in general different from $n < v_{rel}\sigma_{22}^{tr.} >_2$ given with the transport cross section (1) or (2). They could be identical only if the lab frame is identical with the CM frame of colliding particles. For demonstration we consider a very special situation that half particles are moving along the positive $Z-$axis and other half particles along the negative $Z-$axis, and all particles have the same energy E,

$$f(x,p) \propto \delta(p_X)\delta(p_Y)\delta(p_Z - E) + \delta(p_X)\delta(p_Y)\delta(p_Z + E)\,. \tag{28}$$

In this case the lab frame is the CM system for every colliding pair. Thus $p_{1Z}^{'2}/E_1^{'2} = cos^2\theta^*$ and $p_{1Z}^2/E_1^2 = 1$. We then have

$$R_{22}^{tr.} = \frac{3}{2}\, n < v_{rel}\sigma_{22}^{tr.} >_2 \tag{29}$$

with $\sigma_{22}^{tr.}$ defined by (1). It is easy to verify that the result (29) does not depend on the chosen direction of the initial momentum. The only necessary conditions are that all particles move along the same (irrespective of $\pm$ sign) direction and have the same energy. Also, if the momentum isotropy is defined as $< |p_Z|/E >$, $R_{22}^{tr.}$ will be changed to

$$R_{22}^{tr.} = 2n < v_{rel}\sigma_{22}^{tr.} >_2 \tag{30}$$

with $\sigma_{22}^{tr.}$ defined by formula (2).

The reason that we dub $R_{22}^{tr.}$ the transport collision rate becomes now obvious: The expression (26) is more general than the simplified formula $n\sigma^{tr.}$ which is usually denoted as the 'transport collision rate' in the literature [7, 8].

We next discuss the physical meaning of the transport collision rate $R_{22}^{tr.}$. Since $R_{22}^{tr.}$ contributes to momentum isotropization according to (15) and (26), it is reasonable to interpret $R_{22}^{tr.}$ as a rate, at which a particle encounters elastic collisions to become isotropic in momentum space. The inverse of $R_{22}^{tr.}$ is then (for ultrarelativistic particles) the mean path (or time) that a particle should travel to become isotropic, and $R_{22}/R_{22}^{tr.}$ is the average number of collisions which a particle needs to become isotropic.

To confirm this interpretation we calculate $R_{22}^{tr.}$ assuming that the collision angle is isotropicly distributed. We then obtain $R_{22}^{tr.} = R_{22}$ via (29) or (30) for the special case (28): A particle needs only one collision to become isotropic if the distribution of the collision angle is isotropic! A more general case than (28), however, will occur during equilibration. The energy spectrum of particles will also tend to Boltzmann-distribution. A particle with high

energy (which is rare) needs now more than one collision on the average to become isotropic, even if the distribution of the collision angle is isotropic. The reason is that a particle with high energy almost encounters collisions with particles having small energy. The relative velocity of the CM frame to the lab frame is large and thus the Lorentz boost has a strong effect. In the lab frame the momentum deflection of particles with high energy is narrowed in the forward flying direction. On the other hand, particles with small energy is turned to be perpendicular to the flying direction, and thus its momentum deflection is large. The averaged effect of the Lorentz boost on the momentum isotropization of all particles is, however, not trivial and has to be calculated numerically.

The above discussions are based on the implicit assumption that the considered system is static. For an expanding system the situation is more complicated, since particles flow. Collisions not only deflect momentum of particles, but also push particles to flow. Adding the flow part which is exactly the contribution of particle drift to momentum isotropization [see Eq. (15)], momentum degradation of a flowing particle towards isotropy will take a longer time ($\sim \theta_{rel.}$) than the inverse of the transport collision rate, since the transport rate of particle drift is negative in an expanding system.

C. $R^{tr.}_{23}$ and $R^{tr.}_{32}$

Compared with W_{22} in (20), W_{23} has an additional term due to particle production

$$W_{23}(t) = \frac{1}{n}\int \frac{d^3p_1}{(2\pi)^3}\frac{p_{1Z}^2}{E_1^2}\,C_{23} - Q(t)\frac{1}{n}\int \frac{d^3p_1}{(2\pi)^3}\,C_{23}\,. \tag{31}$$

Inserting the explicit formula

$$\begin{aligned} C_{23} \;&= \frac{1}{2E_1}\frac{1}{2!}\int d\Gamma_2 d\Gamma_3 \frac{1}{2!}\int d\Gamma_1^{'} d\Gamma_2^{'}\, f_1^{'} f_2^{'}\,|\mathcal{M}_{1'2'\to 123}|^2 (2\pi)^4\delta^{(4)}(p_1^{'}+p_2^{'}-p_1-p_2-p_3) \\ &\quad -\frac{1}{2E_1}\int d\Gamma_2 f_1 f_2 \frac{1}{3!}\int d\Gamma_1^{'} d\Gamma_2^{'} d\Gamma_3^{'} |\mathcal{M}_{12\to 1'2'3'}|^2\,(2\pi)^4\delta^{(4)}(p_1+p_2-p_1^{'}-p_2^{'}-p_3^{'}) \end{aligned} \tag{32}$$

into Eq. (31), we obtain

$$W_{23}(t) = \frac{3}{2}\,n < v_{rel}\,\tilde{\sigma}_{23} >_2 - n < v_{rel}\frac{p_{1Z}^2}{E_1^2}\,\sigma_{23} >_2 - \frac{1}{2}\,Q(t)\,n < v_{rel}\,\sigma_{23} >_2 \tag{33}$$

with

$$\tilde{\sigma}_{23} := \frac{1}{2s}\frac{1}{3!}\int d\Gamma_1^{'} d\Gamma_2^{'} d\Gamma_3^{'}\,\frac{p_{1Z}^{'2}}{E_1^{'2}}\,|\mathcal{M}_{12\to 1'2'3'}|^2\,(2\pi)^4\delta^{(4)}(p_1+p_2-p_1^{'}-p_2^{'}-p_3^{'})\,. \tag{34}$$

The formula for σ_{23} is just (34) without $p_{1Z}'^2/E_1'^2$. The sum of the first two terms on the right hand side of (33) is equal to the first term on the right hand side of (31). These two terms are expressed similar to those in (26) [multiplying $Q_{eq.} - Q(t)$] for W_{22}. The coefficients in the gain and loss term of momentum isotropization, 3/2 and 1, indicate that in a $2 \to 3$ collision the ratio of the gained to the lost particle number is 3/2. The last term in (33) stems from the pure particle production. The coefficient in this term, 1/2, comes from the sum of the gain and loss term of the production process. For a general $M \to N$ collision the coefficients will be, respectively, N/M, 1 and $(N-M)/M$. Assuming the decomposition

$$< v_{rel} \frac{p_{1Z}^2}{E_1^2} \sigma_{23} >_2 \approx < \frac{p_{1Z}^2}{E_1^2} >< v_{rel} \sigma_{23} >_2 \; = Q(t) \; < v_{rel} \sigma_{23} >_2 \tag{35}$$

and then comparing W_{23} to W_{22} in (26) [multiplying $Q_{eq.} - Q(t)$] we realize that a $gg \to ggg$ collision is a factor of 3/2 more efficient for momentum isotropization than a $gg \to gg$ collision, when $\sigma_{22} = \sigma_{23}$ and $\tilde{\sigma}_{22} = \tilde{\sigma}_{23}$. The physical reason is obvious: A $2 \to 3$ collision brings one more particle towards isotropy than a $2 \to 2$ collision.

For the special distribution function (28) we find a relation between the transport collision rate and the transport cross section (1)

$$R_{23}^{tr.} = \frac{3}{2} \frac{3}{2} n < v_{rel} \sigma_{23}^{tr.} >_2 \; . \tag{36}$$

For scattering processes with isotropicly distributed collision angle one obtains $R_{23}^{tr.} = \frac{3}{2} R_{23}$, where

$$R_{23} = n < v_{rel} \sigma_{23} >_2 \tag{37}$$

denotes the collision rate of a gluon encountering $gg \to ggg$ collisions. We see that Bremsstrahlung effectively shortens the *mean transport path* of particles becoming isotropic in momentum space. Generally, in a $2 \to N$ process

$$R_{2N}^{tr.} = \frac{N}{2} \frac{3}{2} n < v_{rel} \sigma_{2N}^{tr.} >_2 , \tag{38}$$

and the larger the number N, the stronger is the effect.

The final expression of W_{32} (intermediate steps are analogous to those for W_{23} and neglected, and the expression of C_{32} can be found in [5]) is given as

$$W_{32}(t) = \frac{1}{3} n^2 < \frac{\tilde{I}_{32}}{8 E_1 E_2 E_3} >_3 - \frac{1}{2} n^2 < \frac{p_{1Z}^2}{E_1^2} \frac{I_{32}}{8 E_1 E_2 E_3} >_3 + \frac{1}{6} Q(t) \, n^2 < \frac{I_{32}}{8 E_1 E_2 E_3} >_3 , \tag{39}$$

where

$$\tilde{I}_{32} := \frac{1}{2!}\int d\Gamma_1^{'} d\Gamma_2^{'}\, \frac{p_{1Z}^{'2}}{E_1^{'2}}\, |\mathcal{M}_{123\to 1'2'}|^2\, (2\pi)^4 \delta^{(4)}(p_1+p_2+p_3-p_1^{'}-p_2^{'})\,. \tag{40}$$

The formula for I_{32} is just (40) without $p_{1Z}^{'2}/E_1^{'2}$. I_{32} and $\tilde{I}_{32}$ are similar to σ_{23} and $\tilde{\sigma}_{23}$ integrating over all possible states of outgoing particles. $<>_3$ denotes an ensemble average over triplets of incoming particles.

We now compare W_{23} to W_{32}. At first the sum of the last term in (33) and (39) stems from the second term in Eq. (12) with $C_{23}+C_{32}$ instead of $\partial f/\partial t$ and should be zero at chemical equilibrium: We obtain

$$n < v_{rel}\,\sigma_{23} >_2 = \frac{1}{3} n^2 < \frac{I_{32}}{8E_1E_2E_3} >_3 \tag{41}$$

or equivalently $R_{23} = \frac{2}{3} R_{32}$ with

$$R_{32} = \frac{1}{2} n^2 < \frac{I_{32}}{8E_1E_2E_3} >_3 \ . \tag{42}$$

Equation (41) leads to the definition of the collision rate of a gluon encountering $ggg \to gg$ collisions. Assuming a further decomposition besides (35)

$$< \frac{p_{1Z}^2}{E_1^2} \frac{I_{32}}{8E_1E_2E_3} >_3 \approx Q(t)\ < \frac{I_{32}}{8E_1E_2E_3} >_3 \tag{43}$$

we then have finally

$$\begin{aligned} W_{23}(t) &\approx \frac{3}{2}(n < v_{rel}\,\tilde{\sigma}_{23} >_2 - Q(t)\, n < v_{rel}\,\sigma_{23} >_2) \\ W_{32}(t) &\approx \frac{1}{3} n^2 < \frac{\tilde{I}_{32}}{8E_1E_2E_3} >_3 - Q(t) \frac{1}{3} n^2 < \frac{I_{32}}{8E_1E_2E_3} >_3 \ . \end{aligned}$$

These approximate expansions together with Eq. (41) lead to $W_{23} \approx \frac{3}{2} W_{32}$ and $R_{23}^{tr.} \approx \frac{3}{2} R_{32}^{tr.}$ at chemical equilibrium. This demonstrates that a $2 \to 3$ process should contribute more to kinetic equilibration than a $3 \to 2$ process, because it brings one more particle towards isotropy. If the system is out of chemical equilibrium, heuristically one expects $R_{23}^{tr.} \approx \frac{3}{2}\frac{1}{\lambda_g} R_{32}^{tr.}$, where λ_g denotes the gluon fugacity being 1 at chemical equilibrium. In an undersaturated system ($\lambda_g < 1$), for instance, particle production is dominating and thus $R_{23}^{tr.}$ will be much larger than $R_{32}^{tr.}$.

In the special case (28) there is a direct relation between the transport collision rate and transport cross section [see (29) and (36)]. One can also expect such a relation for $R_{32}^{tr.}$ employing the principle of detailed balance. This is

$$R_{32}^{tr.} \approx \frac{2}{3}\,\lambda_g\, R_{23}^{tr.} = \frac{3}{2}\,\lambda_g\, n < v_{rel} \sigma_{23}^{tr.} >_2 \ . \tag{44}$$

If the distribution of the collision angle is isotropic, we have $R^{tr.}_{32} \approx \lambda_g R_{23} = \frac{2}{3} R_{32}$. For the last equality we have used $\lambda_g = 2R_{32}/3R_{23}$. In case of a $N \to 2$ collision ($N > 2$)

$$R^{tr.}_{N2} \approx \frac{2}{N} \lambda_g R^{tr.}_{2N} = \frac{3}{2} \lambda_g n < v_{rel} \sigma^{tr.}_{2N} >_2 \tag{45}$$

which, in contrast to $R^{tr.}_{2N}$ in (38), is not proportional to N. It shows that for large N a $2 \to N$ process is much more efficient for kinetic equilibration than its back reaction.

We summarize the main findings derived in this section:

- The contributions of particle drift and the various collision processes to momentum isotropization are expressed by Eq. (15) which states that the relaxation rate of momentum isotropization is a sum of the *transport rate* of particle drift and the *transport collision rates* of the various scattering processes.

- In an expanding medium the transport rate of particle drift is negative, which just means that particle drift counteracts the momentum isotropization.

- The formulas derived to calculate the transport collision rates of the various interactions, (26), (33) and (39) [over $Q_{eq.} - Q(t)$], are exact and contain implicitly the determinant effects of the distribution of the collision angle on momentum isotropization.

- $2 \to N$ ($N > 2$) processes are most efficient for momentum isotropization compared to elastic collisions or annihilation processes. This is so as a production process brings more than two particles to become isotropic in momentum space.

- For the very special distribution (28) we find the direct relations between the transport collision rates and the transport cross sections:

  $$R^{tr.}_{22} = \frac{3}{2} n < v_{rel} \sigma^{tr.}_{22} >_2 , \; R^{tr.}_{23} = \frac{3}{2} \frac{3}{2} n < v_{rel} \sigma^{tr.}_{23} >_2 , \; R^{tr.}_{32} \approx \frac{3}{2} \lambda_g n < v_{rel} \sigma^{tr.}_{23} >_2 , \tag{46}$$

  if the momentum isotropy is quantified by $< p_Z^2/E^2 >$ and the transport cross section is defined by (1). The relations will be changed to

  $$R^{tr.}_{22} = 2 n < v_{rel} \sigma^{tr.}_{22} >_2 , \; R^{tr.}_{23} = \frac{3}{2} 2 n < v_{rel} \sigma^{tr.}_{23} >_2 , \; R^{tr.}_{32} \approx 2 \lambda_g n < v_{rel} \sigma^{tr.}_{23} >_2 , \tag{47}$$

  if the momentum isotropy is quantified by $< |p_Z|/E >$ and the transport cross section is defined by (2). For the isotropic distribution of the collision angle we obtain in both

cases

$$R_{22}^{tr.} = R_{22}\,, \qquad R_{23}^{tr.} = \frac{3}{2}\,R_{23}\,, \qquad R_{32}^{tr.} \approx \frac{2}{3}\,R_{32}\,. \tag{48}$$

In the following section we will present explicit results on the transport rates of gluons, obtained from the calculations employing the BAMPS, which simulates kinetic parton evolution in a central Au+Au collision at the highest RHIC energy.

VI. RESULTS FROM THE PARTON CASCADE CALCULATIONS

In Fig. 6 (section IV) we have shown the results on momentum isotropization of gluons via the time evolution of the momentum isotropy defined by the average of p_Z^2/E^2 over gluons in the most central region. In the previous section, the contributions of particle drift and the various scattering processes to momentum isotropization are quantified by the transport rates. Detailed expressions of the transport rates can be found in section V and Appendix A. In this section we first present results on the transport rates calculated from the BAMPS simulations. We then compare the transport rates with those obtained from the standard concept of the transport cross sections. In addition, we discuss the applicability of the simple minded relaxation time approximation by determining a potential momentum dependence of the relaxation time.

A. Transport rate

Figure 7 shows the transport rate of particle drift $R_{drift}^{tr.}$ multiplied by -1. At a certain time, $R_{drift}^{tr.}$ is not computed as indicated by Eq. (17) because of a too strong numerical uncertainty in calculating $\vec{\nabla} f$. It is obtained by the explicit sum of $\pm[Q(t) - p_Z^2/E^2]$ over the particles which come in (+ sign) as well as leave (- sign) the central region within a time interval of 0.1 fm/c. The extraction still causes a large statistical fluctuation. The solid and dashed curve in Fig. 7 depict, respectively, $-R_{drift}^{tr.}$ obtained from the simulation with and without the pQCD Bremsstrahlung processes. We realize that the larger the momentum isotropy Q (see Fig. 6), the larger is the (negative) effect of the particle drift on momentum isotropization. This confirms our qualitative understanding outlined in section IV. The dotted curves depict the estimates according to the formula (19), where the one-dimensional expansion with Bjorken's boost-invariance is assumed. $Q(t)$ and $< p_Z^4/E^4 > (t)$

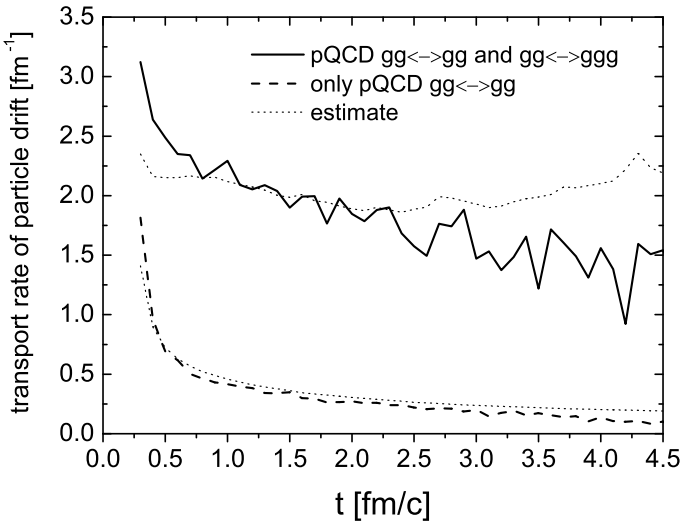

FIG. 7: Transport rate of particle drift (multiplied by -1). Results are obtained, respectively, from the simulation including both elastic and inelastic pQCD scattering processes (solid curve) and from the simulation including only elastic pQCD scattering processes (dashed curve). The dotted curves depict estimates according to Eq. (19).

are calculated from the parton cascade simulations. We see that the estimates nicely meet the numerical results at intermediate times, which indicates that the gluon expansion at these times is well decribed by Bjorken's picture. At very early time the particle drift is stronger due to the early free streaming caused by the particular chosen initial condition. At the later times expansion becomes three-dimensional. In the transverse direction particles also flow outwards. The transverse drift of particles with large p_T is then similar to the longitudinal drift of particles with large $p_Z \sim p_T$. The net effect of the particle drift on the momentum isotropy in a three-dimensional expansion thus becomes smaller compared with that in an only longitudinal expansion, as demonstrated in Fig. 7 via the comparison of the numerical results with the estimates.

The numerical results of the transport collision rates of the various scattering processes are calculated from the BAMPS simulations by using the expressions (26), (33) and (39) [the last two have to be divided by $Q_{eq.} - Q(t)$], and shown in Fig. 8. The thick solid, thick dashed and thick dotted curve depict, respectively, the transport collision rate $R_{22}^{tr.}$, $R_{23}^{tr.}$ and $R_{32}^{tr.}$ calculated in the simulation with both elastic and inelastic pQCD collisions. One realizes the dominance of inelastic collisions in momentum isotropization by computing

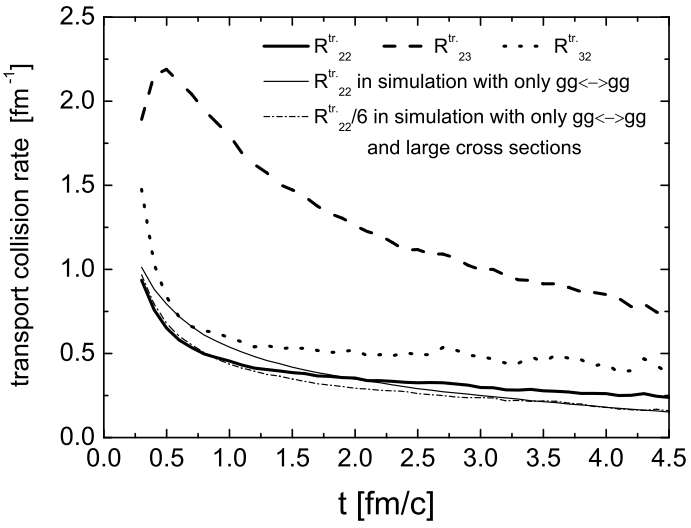

FIG. 8: Transport collision rates of the various scattering processes. $R^{tr.}_{22}$, $R^{tr.}_{23}$ and $R^{tr.}_{32}$ obtained from the simulation including both elastic and inelastic pQCD scattering processes are depicted, respectively, by the thick solid, thick dashed and thick dotted curve. The thin solid (thin dash-dotted) curve show $R^{tr.}_{22}$ ($R^{tr.}_{22}/6$) obtained from the simulation with only elastic pQCD scatterings (with only elastic collisions and using artificially large cross sections).

the ratio $(R^{tr.}_{23} + R^{tr.}_{32})/R^{tr.}_{22}$ which is nearly 5 during the whole evolution. The ratio of $R^{tr.}_{23}$ to $R^{tr.}_{32}$ is always larger than 3/2, but approaches 3/2 at late times. This, according to (44), indicates that the system is rather undersaturated at early times and balancing to chemical equilibrium during the evolution. The thin solid curve in Fig. 8 presents $R^{tr.}_{22}$ in the simulation with only pQCD elastic processes. When comparing this with the thick solid curve one cannot realize the large difference which is seen in the cross sections (compare the solid with the dotted curve in Fig. 4). The reason lies in the different developments of the sceening mass in the different simulations, as shown in Fig. 5. A smaller screening mass leads to a larger cross section on the one hand, but leads to, on the average, a smaller collision angle on the other hand. The former causes frequenter collisions and thus quickens equilibration, while the latter causes inefficient momentum deflection and thus slows down equilibration. Both are convoluted in the transport collision rate which, as it turns out, is thus not so much sensitive to the screening mass as the total cross section does: From Fig. 4 we see that the total cross sections of the elastic collisions in the simulation with only elastic scatterings and in the simulation including the Bremsstrahlung processes differ by a

factor of $4-6$, whereas from Fig. 8 the corresponding transport collision rates are nearly the same.

The ratio of the total transport collision rate in the simulation with both elastic and inelastic pQCD scattering processes, $R_{22}^{tr.}+R_{23}^{tr.}+R_{32}^{tr.}$, to that in the simulation with only elastic pQCD collisions is almost the same as the ratio in the transport rate of particle drift: The ratio increases from 4 at 0.3 fm/c to 9 at 4.5 fm/c. These give, inversely, the same ratio in the timescale of momentum isotropization in both simulations (see also Fig. 11 later in this section).

Since the change in drift of particles is a consequence of collisions among particles, one may expect that the total transport collision rate of various scattering processes is the only quantity determining momentum isotropization. The details of the type of collision processes are not relevant, although they are interesting in their own right. Therefore, kinetic equilibration in all dynamical evolutions of gluons would look the same, if the total transport collision rate in every evolution is the same at every space-time point. We have already shown two examples of the gluon evolution in a central Au+Au collision at RHIC energy. The total transport collision rate becomes, on the average, a factor of 6 larger if the pQCD Bremsstrahlung processes are included. In order to mimic a different gluon evolution having the same total transport collision rate as that obtained in the simulation including the pQCD Bremsstrahlung processes, we have carried out a new simulation with only elastic scattering processes and with larger cross sections than the elastic pQCD cross sections, namely, $d\sigma_{22}/d\hat{t} = 6\, d\sigma_{22}^{pQCD}/d\hat{t}$. The prefactor of 6 would be an appropriate number if the elastic pQCD cross section obtained from the new simulation is exactly the same as that obtained from the simulation with only elastic scatterings and with the pQCD cross section (see the dotted curve in Fig 4). The dash-dotted curve in Fig. 4 shows the elastic pQCD cross section calculated from the new simulation, which is, however, a factor of 2 smaller than the dotted curve. The difference, as mentioned before, stems from the different development of the screening mass (compare the dotted and the dash-dotted curve in Fig. 5). As pointed out in section IV, the gluon evolution in the simulation with only elastic pQCD scatterings resembles that of a free streaming, and the screening mass decreases as $\sim 1/t^{1/2}$. In the new simulation with artificially large cross sections the decrease of the screening mass is between $1/t^{1/2}$ and $1/t^{1/3}$, which indicates that the gluon evolution in the new simulation is a hydrodynamical expansion with a finite viscosity.

The transport collision rate R_{22}^{tr} in the new simulation, divided by 6, is depicted in Fig. 8 by the thin dash-dotted curve and is nearly the same as the transport collision rate (thin solid curve) obtained from the simulation with the standard pQCD cross section. This shows, as already discussed, that the transport collision rate of the elastic pQCD scatterings is not sensitive to the screening mass. Therefore, the total transport collision rates in the new simulation and in the simulation with both elastic and inelastic pQCD scatterings are nearly the same, which implies the same momentum isotropization in both simulations. Comparing the time evolution of the momentum isotropy in both simulations (the solid versus the dotted curve in Fig. 6), we realize that momentum isotropization in both simulations is indeed (also nearly) the same. On the other hand, the total cross sections in the two simulations are very different (see Fig. 4): At the late stage at 4.5 fm/c for instance, $< \sigma_{22} >_2 + < \sigma_{23} >_2 \approx 4$ mb in the simulation including inelastic scatterings, while $< \sigma_{22} >_2 \approx 45$ mb in the new simulation with only elastic collisions, a factor of 12 more, which is unrealistically large.

Since kinetic equilibration and the buildup of pressure relate to each other, we also expect that the buildup of pressure should not depend on the detail of the particular types of interactions either. Figure 9 shows the time evolutions of the transverse energy per unit momentum rapidity at midrapidity, obtained from the three simulations carried out before. The decrease of the transverse energy indicates that mechanical work has been done by pressure gradients which are built up during kinetic equilibration. From Fig. 9 one first realizes that the time evolutions of $dE_T/dy|_{y=0}$ obtained from the simulation with both pQCD elastic and inelastic scatterings (solid curve) and from the new simulation with only elastic scatterings and large cross sections (dash-dotted curve) are almost the same. This indicates that the ongoing kinetic equilibration and the buildup of pressure gradients observed in the two simulations are the same not only at the collision center, as already shown in Fig. 6, but also at the central slice of the expansion. Only the total transport collision rate matters for this finding, but not the detail of the interactions.

We also notice that while the decrease of $dE_T/dy|_{y=0}$ in the simulation with only pQCD elastic collisions (dotted curve) is very weak, which is consistent with the seen very slow momentum isotropization, the decreases of $dE_T/dy|_{y=0}$ in the other two simulations are close to the ideal hydrodynamic limit at least at early times until 1.5 fm/c. At later times the expansion becomes three-dimensional, gluons in the outer regions stop to interact when the energy density there decreases under the critical value of $1\,\mathrm{GeV/fm}^3$. Therefore, the

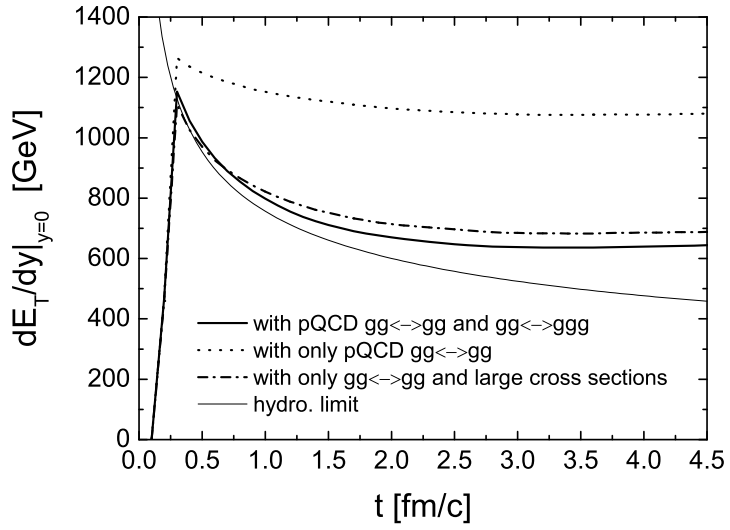

FIG. 9: Time evolution of the transverse energy per unit momentum rapidity at midrapidity. The solid, dotted and dash-dotted curve depict, respectively, the result obtained from the simulation with both pQCD elastic and inelastic scatterings, from the simulation with only pQCD elastic scatterings and from the simulation with only elastic scatterings and large cross sections. The result expected from ideal hydrodynamics, $dE_T/dy|_{y=0} \sim t^{-1/3}$, is shown by the thin solid curve.

decrease of the transverse energy is slowing down. The final value of $dE_T/dy|_{y=0}$ is about 650 GeV which is comparable with the measured data at RHIC [25].

We note that although the details of the interactions among particles do not matter for kinetic equilibration and the buildup of pressure, they do matter for chemical equilibration. Elastic collisions conserve the abosulte number of particles and have no contribution to chemical equilibration, while multiplication and annihilation processes can, in principle, turn a system towards chemical equilibrium. For the present example of the gluon evolution in a central Au+Au collision the initial free streaming (or the off-shell propagation) brings the gluon system into an undersaturated state (see later Fig. 14). In the simulation including the pQCD Bremsstrahlung processes chemical equilibrium is achieved by producing gluons. This leads to a larger screening mass than that in the simulations with only elastic collisions (compare the solid curve with the other curves in Fig. 5). Therefore, the elastic pQCD cross section obtained from the simulation including the pQCD Bremsstrahlung processes is the smallest compared to those obtained from the other simulations (see Fig. 4).

B. Mean free path, mean transport path and relaxation time

Figure 10 shows the mean free path of gluons by thick curves and the *mean transport path* by thin curves obtained from the three different simulations. Remember that the *mean*

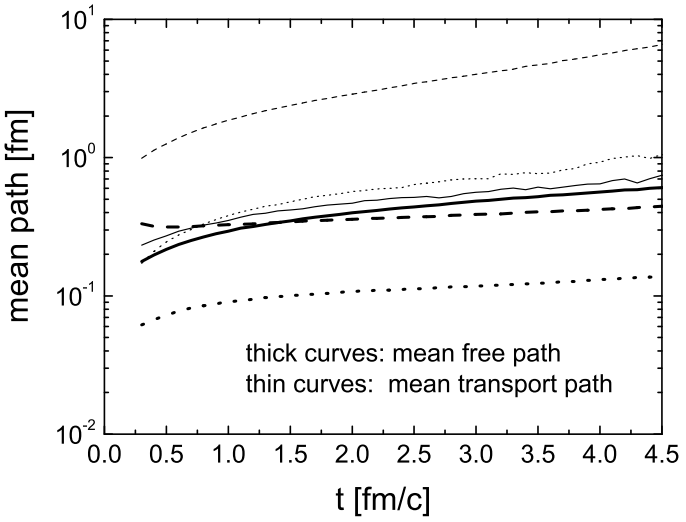

FIG. 10: Mean free path and mean transport path of gluons. The thick (thin) solid, dashed and dotted curves depict, respectively, the mean free path (the mean transport path) obtained from the simulation including both elastic and inelastic pQCD scattering processes, from the simulation with only elastic pQCD scatterings and from the simulation with only elastic collisions and with artificially large cross sections.

transport path is just the inverse of the total transport collision rate which a gluon needs to travel in a static medium to become isotropic in momentum space. From Fig. 10 we see that both mean pathes in all the simulations are small at early times and increase in the course of expansion when the system becomes dilute. Comparing the mean free pathes in the different simulations one recognizes that they do not differ very much in the simulations with and without the pQCD Bremsstrahlung processes, while it is much smaller in the simulation with artificially large cross sections. The differences in the total transport collision rates obtained from the different simulations are already discussed in the previous subsection. We plot the mean transport pathes into Fig. 10 for the comparison with the mean free pathes. We see that the mean transport path is much larger than the mean free path in both simulations with only elastic collision processes. This reflects the fact that the elastic pQCD collisions are small-angle scatterings and thus are not efficient for momentum isotropization. On the

contrary, the mean transport path and the mean free path in the simulation including the pQCD Bremsstrahlung processes are rather close to each other. This shows the efficiency of the pQCD Bremsstrahlung processes and their back reactions for kinetic equilibration.

The inverse of the relaxation time, the relaxation rate $1/\theta_{rel.}(t)$ of the momentum isotropy, is calculated directly from Fig. 6 by expression (9), and is shown in Fig. 11 compared with the total transport rate $R^{tr.}_{drift} + R^{tr.}_{22} + R^{tr.}_{23} + R^{tr.}_{32}$. They should be identical according

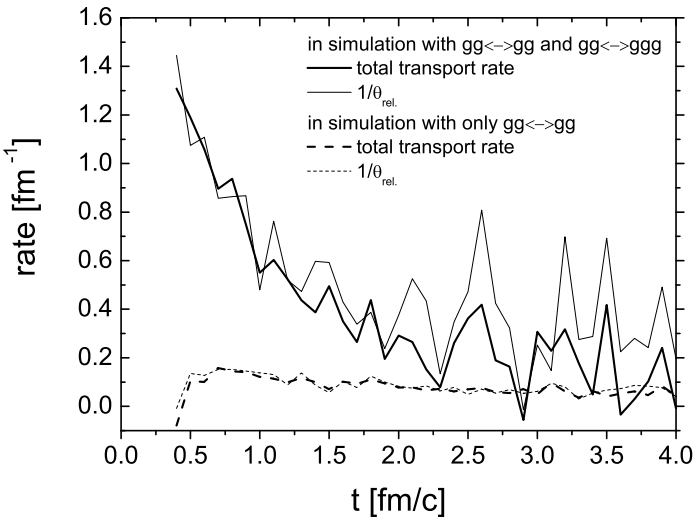

FIG. 11: Relaxation rate of the momentum isotropy compared with the total transport rate. The thick solid (thick dashed) curve depicts the total transport rate obtained from the simulation including both elastic and inelastic pQCD scattering processes (only elastic pQCD processes), while the thin solid (thin dashed) curve shows the relaxation rate $1/\theta_{rel.}(t)$ calculated by (9).

to (15). Indeed, we see that within the numerical uncertainty the total transport rate is equal to the relaxation rate of the momentum isotropy, which indicates the correct numerical extractions of the separate transport rate. One can also realize that for the first 2 fm/c of the gluon evolution including the pQCD Bremsstrahlung processes, the timescale of momentum isotropization is $1 - 2$ fm/c, which is a factor of about 5 larger than the mean free path (compared with the thick solid curve in Fig. 10).

C. Collision rate, transport collision rate and transport cross section

In this subsection we look into the details of the various scattering processes by comparing the collision rates, the transport collision rates and the estimates relating to the transport

cross sections with each other. We concentrate on the results from the simulation with both elastic and inelastic collisions.

We have seen in section V that only in the very limiting case (28) the transport collision rates can be reduced to the formulas being directly proportional to the transport cross sections [see also (46), (47) and (48)]. However, in principle, the formulas via the transport cross sections [7, 8] give more simple relations to the distribution of the collision angle. It is interesting to know how they might differ from the true transport collision rates in the course of the gluon evolution in a heavy-ion collision at RHIC. In Fig. 12 we show the comparisons of the collision rates (solid curves), the transport collision rates (dashed curves) and $n < v_{rel}\,\sigma^{tr.} >$ (dotted curves) with each other. The respective multiplication factors

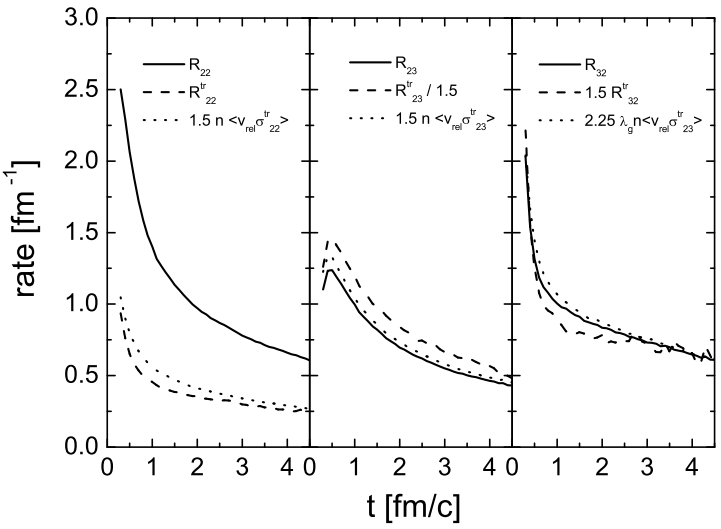

FIG. 12: Collision rate, transport collision rate and $n < v_{rel}\,\sigma^{tr.} >$ of the various collision processes. The results are obtained from the simulation including both elastic and inelastic pQCD scattering processes, and are depicted by the solid, dashed and dotted curves respectively.

serve to make convenient comparisons according to (46) and (48): If the real situation is like the special situation (28), the dashed and the dotted curves would lie exactly on top of each other. If additionally the distribution of the collision angle is isotropic, all the curves in each panel would lie on top of each other. The fugacity λ_g entered in the last expression in (46) is calculated by $\lambda_g = n/n_{eq.}$, where $n_{eq.} = 16\,T^3/\pi^2$ is the gluon density at thermal equilibrium at the current temperature obtained by $T \equiv \epsilon/3n$. The current gluon density n and energy density ϵ are extracted from the parton cascade simulation.

First we look at the rates of the elastic scattering processes (left panel in Fig. 12). There is only a small difference between the true transport collision rate (dashed curve) and the reduced rate relating to the transport cross section (dotted curve). The difference stems from the effect of Lorentz boost from the CM frame to the lab frame, as discussed in section V. Furthemore, we see that the transport collision rate is much smaller than the collision rate (solid curve), which again is due to the fact that the pQCD $gg \to gg$ scatterings are small-angle scatterings and are not efficient for momentum isotropization.

For the $gg \to ggg$ Bremsstrahlung processes (middle panel) all the curves do not differ very much from each other. The transport collision rate divided by the kinematic factor 3/2 is the largest and particularly larger than the collision rate. This indicates that the Bremsstrahlung processes favor large-angle emission. On the other hand, the kinematic factor which is exactly 3/2 in the special case (28) is only approximately equal to 3/2 in general case, because the decomposition (35) for $R_{23}^{tr.}$ [see $W_{23}^{tr.}$ in (33)] is an approximation. The real kinematic factor could be larger than 3/2, which could bring the dashed curve below the solid curve. Even though, the difference between the transport collision rate divided by 3/2 and the collision rate is small. This shows that the distribution of the collision angle in the $gg \to ggg$ collisions is nearly isotropic. The same is also seen in the right panel of Fig. 12, where all the rates concerning the $ggg \to gg$ processes are nearly the same.

From Fig. 12 we have noticed that the reduced transport collision rates relating to the transport cross sections do not differ very much from the exactly derived transport collision rates. It seems that on the average, the Lorentz boost from the individual CM frame to the lab frame does not lead to a big effect on momentum isotropization. The nice approximate agreement with the reasoning in section V is not trivial. However, it clearly provides a basis to understand thermalization within multiparticle reactions. In addition, as proven now, the derivation of the transport collision rates is very useful to obtain the *kinematic* factors in the expressions (46), which are essential in quantitative analyses and typically are ignored in the literature [7, 8].

The roughly isotropic distribution of the collision angle in the $gg \leftrightarrow ggg$ processes is due to the simple minded implementation of the LPM effect which stems from the interference of the radiated gluons (originally photons in the QED medium) by multiple scatterings of a parton though a QCD medium. This coherent effect leads to suppression of radiation of gluons with certain modes $(w, \vec{k})$, where w and $\vec{k}$ denote energy and momentum of a

gluon respectively. Heuristically, there is no suppression for gluons with a *formation time* $\tau = w/k_T^2$ smaller than the mean free path. This is called the Bethe-Heitler limit where the gluon radiations induced at a different space-time point in the course of the propagation of a parton can be considered as independent events. These events within the Bethe-Heitler regime have been included in the present BAMPS calculations. On the other hand, radiations of other gluon modes with coherent suppression completely drop out, which is indicated by the Θ-function in the matrix element (4). The inclusion of those radiations would speed up thermalization. How to implement the coherent effect into a transport model solving the Boltzmann equation is still a challenge. The Θ-function in the matrix element (4) results in a cut-off for the transverse momentum k_T of the radiated gluon, namely $k_T > 1/\Lambda_g$, where Λ_g is the mean free path of a gluon. A larger value of the cut-off will decrease the total cross section of a $gg \to ggg$ collision approximately logarithmically on the one hand [see (4)] and makes the collision angle larger on the other hand. The latter leads to a larger efficiency for momentum isotropization. Varying the cut-off downwards to a smaller value one would enter into the LPM suppressed regime. Detailed analyses on the sensitivity of the k_T cut-off to thermalization will be given in a future work.

D. Independence of the transport rate on the definition of the momentum isotropy

We have already mentioned in section V that the formulas derived to calculate the transport rates depend on how the momentum isotropy is defined. In the previous subsections the numerical results on the transport rates concerning the momentum isotropy $< p_Z^2/E^2 >$ defined by expression (10) were shown. The question which still has to be addressed is how the numerical results of the transport rates change, if for instance, the momentum isotropy is defined by $< |p_Z|/E >$.

Since any reasonable definition of the momentum isotropy represents some kind of average of the momentum spectra shown in Fig. 2, the timescale of momentum isotropization, obtained from different prescriptions, cannot differ much from each other. We know that the inverse of the total transport rate is just the timescale of momentum isotropization. Therefore, we do not expect any significant large dependence of the transport rates on the particular definition of the momentum isotropy.

For the present case we first compare the transport collision rates, approximated by the

reduced formulas (46) concening the momentum isotropy $< p_Z^2/E^2 >$, with those in (47) concerning $< |p_Z|/E >$. The transport cross sections are defined by (1) and (2) respectively. We have already shown that if the collsion angle is isotropic distributed, the transport collision rates of a certain type of scattering processes are the same, irrespective of the different definition of the momentum isotropy. For small-angle scatterings one has $\sin^2\theta \approx \theta^2$ and $1-\cos\theta \approx \theta^2/2$. In this case the transport collision rates concerning $< p_Z^2/E^2 >$ are a factor of 1.5 larger than those concerning $< |p_Z|/E >$. On the other hand, $\sin^2\theta \approx 1-\cos\theta$ for large-angle scatterings. The transport collision rates concerning $< p_Z^2/E^2 >$ are in turn a factor of 3/4 smaller than those concerning $< |p_Z|/E >$. The maximal relativ difference amounts to 50%. Since the pQCD Bremsstrahlung emission is the dominant process in kinetic equilibration, and the collision angle for that process is roughly isotropic due to the LPM cut-off, the difference in the transport collision rates due to different definition of the momentum isotropy should be small.

Figure 13 shows the numerical results on the transport rates (obtained from the BAMPS calculations) with the two different prescriptions of the momentum isotropy. The solid curves

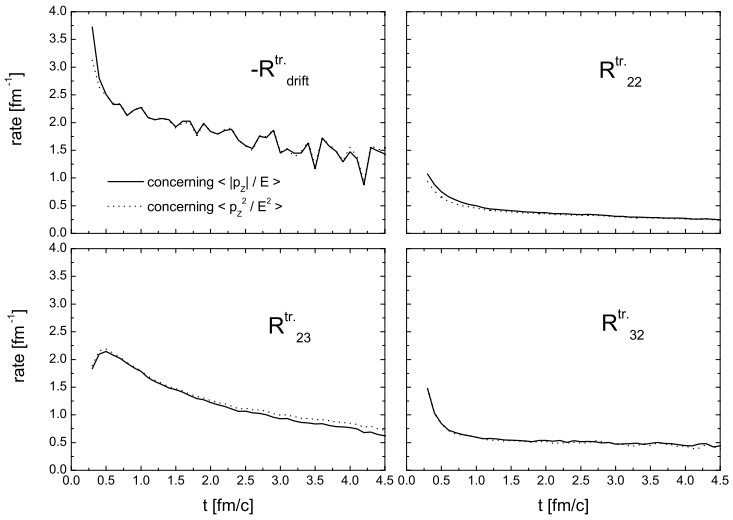

FIG. 13: Transport rates calculated with different definitions of the momentum isotropy. The solid curves depict the results concerning $< |p_Z|/E >$, while the dotted curves depict those concerning $< p_Z^2/E^2 >$.

depict the results concerning $< |p_Z|/E >$, while the dotted curves depict those concerning $< p_Z^2/E^2 >$, which have been already shown in Figs. 7 and 8. One indeed sees only tiny

differences for each type of processes. This demonstrates the independence of the achieved results on the particular definition of the momentum isotropy.

E. Relaxation time $\tau_{rel.}$ in the relaxation time approximation

The collision term of the Boltzmann equation (13) can, in principle, always be written as

$$C(x,p) = \frac{f_{eq.}(x,p) - f(x,p)}{\tau_{rel.}(x,p)} \tag{49}$$

which describes the relaxation of the particle density function $f(x,p)$ by using a space-time and momentum dependent *relaxation time* $\tau_{rel.}(x,p)$. On the other hand, $\tau_{rel.}(x,p)$ is a rather involved functional of $f(x,p)$. We denote the relaxation time by $\tau_{rel.}$ to avoid confusion with $\theta_{rel.}$. The underlying approximation in the so-called *relaxation time ansatz* is the *ignorance* of the momenum dependence of the relaxation time, i.e., $\tau_{rel.}(x,p) \approx \tau_{rel.}(x)$. $\tau_{rel.}$ thus gives the timescale of overall equilibration in absence of particle drift. Many works [9, 10, 11, 12, 13, 14, 15] are done by employing the relaxation time approximation to calculate the timescale of thermalization within the various dynamical scenarios of the expansion. Based on the analyses on the transport rate so far, it is of crucial interest to see whether or not $\tau_{rel.}$ in the relaxation time approximation is equivalent to the mean transport path. Remember that the latter, as realized in section V, determines the timescale of momentum isotropization for a static system.

For kinetic equilibration we insert (49) into the time derivative of the momentum isotropy (12) and obtain (by dividing $Q_{eq.} - Q$)

$$\begin{aligned} R_{22}^{tr.} + R_{23}^{tr.} + R_{32}^{tr.} &= \frac{1}{Q_{eq.} - Q}\left(\frac{1}{n}\int \frac{d^3p}{(2\pi)^3}\frac{p_Z^2}{E^2}\frac{f_{eq.} - f}{\tau_{rel.}} - Q(t)\frac{1}{n}\int \frac{d^3p}{(2\pi)^3}\frac{f_{eq.} - f}{\tau_{rel.}}\right) \\ &= \frac{1}{Q_{eq.} - Q}\left(\frac{n_{eq.}\,Q_{eq.} - n\,Q}{n \;<\tau_{rel.}>_k} - Q\frac{n_{eq.} - n}{n \;<\tau_{rel.}>_c}\right). \end{aligned} \tag{50}$$

So far everything is exact by introducing $<\tau_{rel.}>_k$ and $<\tau_{rel.}>_c$ which are the averaged quantities over momentum. The index k denotes kinetic equilibration due to the convolution of angles (p_Z^2/E^2) in the first integration, while c denotes chemical equilibration.

$<\tau_{rel.}>_c$ can be also calculated by integrating the collision term of the Boltzmann equation over momentum

$$\int \frac{d^3p}{(2\pi)^3}\left(C_{22} + C_{23} + C_{32}\right) = \int \frac{d^3p}{(2\pi)^3}\frac{f_{eq.} - f}{\tau_{rel.}} = \frac{n_{eq.} - n}{<\tau_{rel.}>_c}. \tag{51}$$

Sometimes this is taken as a standard, but very simple minded ansatz for the relaxation time [13]. The left hand side of the above equation is equal to $n(R_{23}/2 - R_{32}/3)$ if applying the explicit formulas of the collision terms and the definition of the collision rates. We then obtain

$$< \tau_{rel.} >_c = \frac{1/\lambda_g - 1}{R_{23}/2 - R_{32}/3}\,, \tag{52}$$

where $\lambda_g = n/n_{eq.}$ denotes the gluon fugacity.

Assuming the approximation that the relaxation time is independent on momentum, $< \tau_{rel.} >_k$ and $< \tau_{rel.} >_c$ are equal and one gets from Eq. (50)

$$< \tau_{rel.} >_k = \frac{1}{\lambda_g}\,\frac{1}{R_{22}^{tr.} + R_{23}^{tr.} + R_{32}^{tr.}}\,. \tag{53}$$

At chemical equilibrium ($\lambda_g = 1$) the relaxation time, under the strict assumption of the independence of momentum, is just the inverse of the total transport collision rate, or, the mean transport path. However, it is not obvious why the right hand side of Eqs. (52) and (53) should be equal.

On the other hand, we can exactly calculate the $< \tau_{rel.} >_c$ and $< \tau_{rel.} >_k$ using (52) and (50), since all the collision rates and the transport collision rates are already known from the numerical simulations. If the two 'relaxation times' differ very much from each other, one can conclude that the relaxation time $\tau_{rel.}(x,p)$ is strongly momentum dependent and cannot serve as a global quantity determining the timescale of overall thermalization of gluons in ultrarelativistic heavy-ion collisions.

Before we perform calculations for $< \tau_{rel.} >_c$ and $< \tau_{rel.} >_k$, we have to manifest the particle density function in equilibrium, $f_{eq.}(x,p)$. Since the quantum effect like the gluon enhancement is neglected in this study, $f_{eq.}(x,p)$ is given by $\nu e^{-E/T}$ for the medium at the collision center. $\nu = 16$ is the degeneracy of gluons. The temperature T can be defined by the requirement $\epsilon_{eq.} = \epsilon$ which stems from the energy conservation in a sudden thermalization [9]. On the other hand, the current particle density function could have an exponential shape, $f = \lambda_g\, f_{eq.}$, for instance, in a case that kinetic equilibration progresses much faster than chemical equilibration. In this case one obtains $n = \lambda_g\, n_{eq.}$ as well as $\epsilon = \lambda_g\, \epsilon_{eq.}$. The temperature is then $T = \epsilon_{eq.}/3n_{eq.} = \epsilon/3n$. It is larger (or smaller) than the temperature defined in the former case, if λ_g is smaller (or larger) than 1. These two *different* definitions of the local temperature lead to the difference in $\epsilon_{eq.}$, $n_{eq.}$ and especially in the gluon fugacity $\lambda_g = n/n_{eq.}$. We denote the case of a sudden thermalization by S and denotes the second

case with an exponential shape of f by E, it is easy to verify that

$$\lambda_g^E = (\lambda_g^S)^4 = \frac{27\pi^2}{16}\,\frac{n^4}{\epsilon^3}\,. \tag{54}$$

They differ from each other with a power of 4. The time evolution of the gluon fugacity λ_g^S and λ_g^E obtained from the simulation including the pQCD Bremsstrahlung processes is shown in Fig. 14 by the dashed and solid curve. We see that although the system of

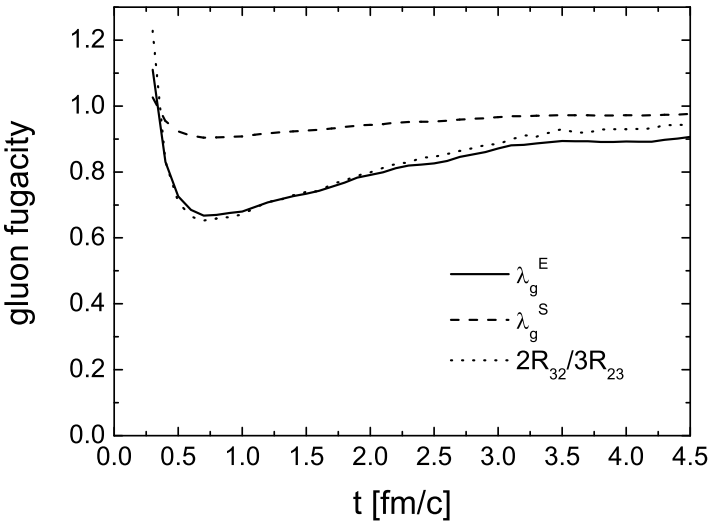

FIG. 14: Gluon fugacity. The solid, dashed and dotted curve depict, respectively, λ_g^E, λ_g^S and $2R_{32}/3R_{23}$ obtained from the simulation including elastic and inelastic pQCD Bremsstrahlung processes.

minijets is initially slightly oversaturated, it becomes undersaturated due to a short period of (quasi)free streaming. The reasoning is obvious according to (54), when n as well as ϵ decreases as $1/t$ in a free streaming. The decrease of λ_g^E is roughly a factor of 4 stronger than that of λ_g^S. We also see that while λ_g^E increases and relaxes to 1 at late times, which indicates the ongoing chemical equilibration, λ_g^S is nearly 1 during the whole expansion, which shows that the system is rather close to chemical equilibrium within this definition. The difference between λ_g^S and λ_g^E comes from (54): $(\lambda_g^E - 1) \approx 4(\lambda_g^S - 1)$ for $|\lambda_g^S - 1| \ll 1$.

From a physical point of view, fugacity is a quantity which balances the particle production and annihilation. Therefore, the ratio of the annihilation rate R_{32} to the production rate R_{23} can serve as a quantitative measure of fugacity. In Fig. 14 we therefore also depict $2R_{32}/3R_{23}$ obtained from the same numerical simulation as for λ_g^E and λ_g^S. We see that

$2R_{32}/3R_{23}$ agrees well with λ_g^E, which implies that λ_g^E would be the appropriate choice for the fugacity in the example of gluon evolution in heavy-ion collisions.

We now calculate the exact momentum averaged 'relaxation time' $< \tau_{rel.} >_k$ and $< \tau_{rel.} >_c$ according to (50) and (52) without any approximations. Figure 15 shows the results obtained by using the different definitions of gluon fugacity. Also the mean transport path,

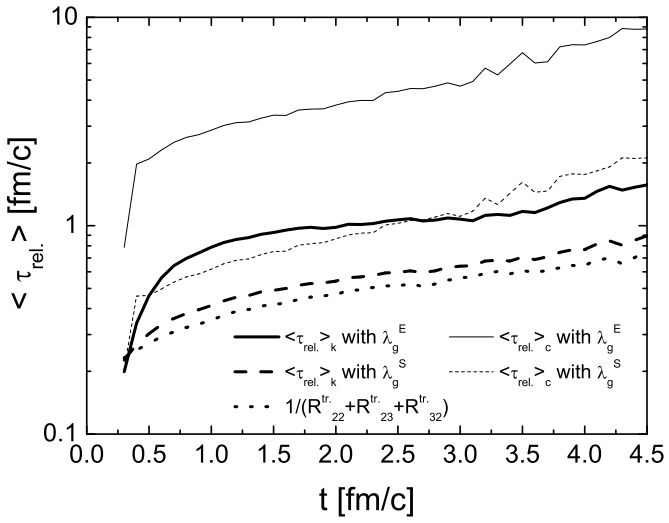

FIG. 15: Relaxation time. The thick (thin) solid curve depicts the momentum averaged 'relaxation time' $< \tau_{rel.} >_k$ ($< \tau_{rel.} >_c$) using the fugacity λ_g^E. The thick (thin) dashed curve depicts $< \tau_{rel.} >_k$ ($< \tau_{rel.} >_c$) using the fugacity λ_g^S. The dotted curve shows again the mean transport path (see Fig. 10). Results are obtained from the simulation including both elastic and inelastic pQCD scattering processes.

$1/(R_{22}^{tr.} + R_{23}^{tr.} + R_{32}^{tr.})$, is depicted for comparisons. We note first that except $< \tau_{rel.} >_k$ with λ_g^S the other 'relaxation times' are considerably much larger than the mean transport path. When now comparing $< \tau_{rel.} >_k$ with $< \tau_{rel.} >_c$, obtained by using the same fugacity, one also realizes large differences, especially for the case when using λ_g^E. Here both 'relaxation times' deviate by a factor of 4 to 6. This implies that the relaxation time $\tau_{rel.}(x,p)$ in (49) indeed has a strong dependence on momentum. We therefore conclude that the applicability of the approximation $\tau_{rel.}(x,p) \approx \tau_{rel.}(x)$ in studying thermalization of gluons in heavy-ion collisions is questionable.

VII. SUMMARY

Employing our recently developed parton cascade BAMPS including the pQCD inelastic Bremsstrahlung processes we have introduced and calculated the transport rate of gluon drift and the transport collision rates of the various scattering processes concerning momentum isotropization within relativistic kinetic theory. The major question addressed is how to understand the observed fast equilibration of gluons within the BAMPS in theoretical terms.

We have shown that the derived transport rate of a certain process, $R^{tr.}_{drift}$, $R^{tr.}_{22}$, $R^{tr.}_{23}$ or $R^{tr.}_{32}$, determines exactly the contribution of the process to the defined momentum isotropization, the ensemble average of p_Z^2/E^2 (or $|p_Z|/E$). The total transport collision rate, $R^{tr.}_{22} + R^{tr.}_{23} + R^{tr.}_{32}$, is the key quantity describing momentum isotropization, while the change of gluon drift is a consequence of collision processes, and $R^{tr.}_{drift}$ is negative in an expanding system. The inverse of the total transport rate, $1/(R^{tr.}_{drift} + R^{tr.}_{22} + R^{tr.}_{23} + R^{tr.}_{32})$, gives exactly the timescale of momentum isotropization $\theta_{rel.}$ which is about 1 fm/c obtained from the BAMPS for the gluon matter produced at RHIC. It is also shown that the calculated transport rates are independent on the definition of the momentum isotropy.

We have also derived the reduced transport collision rates relating to the transport cross sections. They are only exact for a special case when the center-of-mass frame of individual collisions coincides with the lab frame where the medium is observed. The deviations from the exact transport collision rates stem from the effect of Lorentz boosts from the center-of-mass frames to the lab frame. The numerical results have shown that the reduced rates do not differ very much from the exact in the given case of the gluon evolution in a relativistic heavy-ion collision. Lorentz boost seems not to lead to a major effect on momentum isotropization. Nevertheless, the derivation of the transport collision rate is very useful to obtain the correct kinematical factors in the reduced rates summarized in (46), which are essential for a quantitative understanding. These have been typically ignored in the literature. For instance, our analyses showed that a $2 \to N$ $(N > 2)$ production process is about a factor of $(N-2)/2$ more efficient for momentum isotropization than its back reaction as well as an elastic scattering process.

Based on the numerical results of the transport collision rates of the various scattering processes, we have investigated the importance of including the pQCD Bremsstrahlung processes to thermalization. The results showed that the inclusion of the pQCD Bremsstrahlung

processes and their back reactions, as implemented in the BAMPS, increases the efficiency for thermalization by a factor of 5. Overall kinetic equilibration and buildup of pressure happen at a timescale of about 1 fm/c. The large efficiency stems only partly from the increase of the particle number in the final state of $gg \to ggg$ collisions, but mainly from the almost isotropic angular distribution in the Bremsstrahlung process due to the effective implementation of the LPM suppression. The detailed understanding of the latter has to be developed in future investigations.

In addition, we have also calculated the momentum averaged 'relaxation times' within the different prescriptions. It turns out that they differ significantly from each other. This indicates a strong momentum dependence of the gluon relaxation time $\tau_{rel.}$ in the given case of heavy-ion collisions. The applicability of approximating the full kinetic Boltzmann process within the standard relaxation time approximation is thus questionable.

Acknowledgments

The authors thank B. Müller for raising the overall question of analyzing the timescale of thermalization within the present kinetic parton cascade BAMPS. We are indebted to M. Gyulassy for enlightening discussions. C.G. thanks the Galileo Galilei Institute for Theoretical Physics for the hospitality and the INFN for partial support during the completion of this work.

APPENDIX A: MOMENTUM ISOTROPY IN THE CENTRAL REGION

The central region in the present calculation is defined as a cylinder with a radius of $r_b = 1.5$ fm and a longitudinal extension of $2Z_b$. The longitudinal boundary $Z_b = \tanh \eta_b \, t$ with $\eta_b = 0.2$ increases linearly with time. Within the central region the momentum isotropy is defined by

$$\begin{aligned} Q(t) : &= \frac{1}{n} \int \frac{d^3p}{(2\pi)^3} \frac{p_Z^2}{E^2} \frac{1}{V} \int_0^{r_b} dr\, r \int_0^{2\pi} d\phi \int_{-Z_b}^{Z_b} dz\, f(\vec{x}, t, p) \\ &= \frac{1}{n} \int \frac{d^3p}{(2\pi)^3} \frac{p_Z^2}{E^2} \frac{2}{V} \int_0^{r_b} dr\, r \int_0^{2\pi} d\phi \int_0^{Z_b} dz\, f(\vec{x}, t, p)\,, \end{aligned} \tag{A1}$$

where

$$n(t) = \int \frac{d^3p}{(2\pi)^3} \frac{2}{V} \int_0^{r_b} dr\, r \int_0^{2\pi} d\phi \int_0^{Z_b} dz\, f(\vec{x}, t, p)\,. \tag{A2}$$

$V = 2\pi r_b^2 Z_b$ is the volume of the central region. The latter equality in (A1) is due to the symmetry of $f(\vec{x}, t, p)$ under $\vec{x} \to -\vec{x}$ exchange. In the limit $r_b \to 0$ and $\eta_b \to 0$ one has

$$\frac{1}{V}\int_0^{r_b} dr\, r \int_0^{2\pi} d\phi \int_{-Z_b}^{Z_b} dz\, f(\vec{x}, t, p) \to f(\vec{x}, t, p)|_{\vec{x}=0}\,, \tag{A3}$$

and one then obtains the definition of the local momentum isotropy in this limit [see (10) in section V]. The expressions of the transport rates in this limit have been given in section V.

Taking the derivative of $Q(t)$ in time gives

$$\begin{aligned}\dot{Q}(t) \;=\; & \frac{1}{n}\int \frac{d^3p}{(2\pi)^3}\frac{p_Z^2}{E^2}\,\frac{2}{V}\int_0^{r_b} dr\, r \int_0^{2\pi} d\phi \left[\int_0^{Z_b} dz\,\frac{\partial f}{\partial t} + \tanh\eta_b\, f(\vec{x}_\perp, Z_b, t, p)\right] \\ & -Q(t)\frac{1}{n}\int \frac{d^3p}{(2\pi)^3}\frac{2}{V}\int_0^{r_b} dr\, r \int_0^{2\pi} d\phi \left[\int_0^{Z_b} dz\,\frac{\partial f}{\partial t} + \tanh\eta_b\, f(\vec{x}_\perp, Z_b, t, p)\right]\,. \end{aligned} \tag{A4}$$

The second terms in the brackets come from the time derivatives of the boundary Z_b and can be simply rewritten to

$$\tanh\eta_b\, f(\vec{x}_\perp, Z_b, t, p) = \int_0^{Z_b} dz\,\frac{\tanh\eta_b}{Z_b} f(\vec{x}_\perp, Z_b, t, p) = \int_0^{Z_b} dz\,\frac{1}{t} f(\vec{x}_\perp, Z_b, t, p)\,. \tag{A5}$$

Taylor expansion of $f(\vec{x}_\perp, Z_b, t, p)$ at $\vec{x}$ to the first order yields

$$f(\vec{x}_\perp, Z_b, t, p) \simeq f(\vec{x}, t, p) + \frac{\partial f(\vec{x}, t, p)}{\partial z}\,(Z_b - z) \tag{A6}$$

and we obtain

$$\begin{aligned}\dot{Q}(t) \;\simeq\; & \frac{1}{n}\int \frac{d^3p}{(2\pi)^3}\frac{p_Z^2}{E^2}\,\frac{2}{V}\int_0^{r_b} dr\, r \int_0^{2\pi} d\phi \int_0^{Z_b} dz\,\left[\frac{\partial f}{\partial t} + \frac{(Z_b - z)}{t}\,\frac{\partial f}{\partial z}\right] \\ & -Q(t)\frac{1}{n}\int \frac{d^3p}{(2\pi)^3}\frac{2}{V}\int_0^{r_b} dr\, r \int_0^{2\pi} d\phi \int_0^{Z_b} dz\,\left[\frac{\partial f}{\partial t} + \frac{(Z_b - z)}{t}\,\frac{\partial f}{\partial z}\right]\,. \end{aligned} \tag{A7}$$

The contributions (from the two brackets) of the zero-order term in the expansion (A6) cancel due to the definition of $Q(t)$. $(Z_b - z)/t$ expresses the relative velocity of the boundary slice at Z_b to the slice at z where particles are sitting. The second terms in the brackes appear due to the timely increasing longitudinal boundary of the central region, and become smaller when $Z_b \to 0$ (or $\eta_b \to 0$). According to the Boltzmann equation (13) the expression in the brackets can be written to

$$\frac{\partial f}{\partial t} + \frac{(Z_b - z)}{t}\,\frac{\partial f}{\partial z} = -\frac{p_X}{E}\frac{\partial f}{\partial x} - \frac{p_Y}{E}\frac{\partial f}{\partial y} - \left(\frac{p_Z}{E} - \frac{Z_b - z}{t}\right)\frac{\partial f}{\partial Z} + C_{22} + C_{23} + C_{32}\,. \tag{A8}$$

$p_Z/E - (Z_b - z)/t$ means that only particles with longitudinal velocity p_Z/E larger than the relative velocity of the boundary slice $(Z_b - z)/t$ can drift out of the central region. This will be taken into account when calculating the transport rate of particle drift within the central region. The evaluations of the transport collision rates $R_{22}^{tr.}$, $R_{23}^{tr.}$ and $R_{32}^{tr.}$ are more straightforward. One only needs to replace the expressions derived in the limit $r_b \to 0$ and $\eta_b \to 0$, which are already given in section V, by

$$R_i^{tr.} \to \frac{1}{V} \int_0^{r_b} dr\, r \int_0^{2\pi} d\phi \int_{-Z_b}^{Z_b} dz\, R_i^{tr.}\,, \tag{A9}$$

where $i = 22$, 23 or 32.

---

[1] M. Gyulassy and L. McLerran, Nucl. Phys. A **750**, 30-63 (2005).

[2] P. Huovinen, P.F. Kolb, U.W. Heinz, P.V. Ruuskanen and S.A. Voloshin, Phys. Lett. B **503**, 58 (2001).

[3] S.S. Adler et al. [PHENIX Collaboration], Phys. Rev. Lett. **91**, 182301 (2003).

[4] J. Adams et al. [STAR Collaboration], Phys. Rev. Lett. **92**, 052302 (2004).

[5] Z. Xu and C. Greiner, Phys. Rev. C **71**, 064901 (2005).

[6] Z. Xu and C. Greiner, Proceedings of Quark Matter 2006, Nucl. Phys. A **774**, 787-790 (2006).

[7] P. Danielewicz and M. Gyulassy, Phys. Rev. D **31**, 53 (1985).

[8] M.H. Thoma, Phys. Rev. D **49**, 451 (1994).

[9] G. Baym, Phys. Lett. B **138**, 18 (1984).

[10] A. Hosoya and K. Kajantie, Nucl. Phys. B **250**, 666 (1985).

[11] S. Gavin, Nucl. Phys. B **351**, 561 (1991).

[12] H. Heiselberg, Xin-Nian Wang, Phys. Rev. C **53**, 1892 (1996).

[13] S.M.H. Wong, Nucl. Phys. A **607**, 442-456 (1996).

[14] A. Dumitru and M. Gyulassy, Phys. Lett. B **494**, 215 (2000).

[15] J. Serreau and D. Schiff, J. High Energy Phys. **0111**, 039 (2001).

[16] P. Danielewicz and G.F. Bertsch, Nucl. Phys. A **533**, 712 (1991).

[17] A. Lang, H. Babovsky, W. Cassing, U. Mosel, H.G. Reusch, and K. Weber, J. Comp. Phys. **106**, 391 (1993).

[18] W. Cassing, Nucl. Phys. A **700**, 618 (2002).

[19] D. Molnar, Proceedings of Quark Matter 1999, Nucl. Phys. A **661**, 205-260 (1999).

[20] J.F. Gunion and G. Bertsch, Phys. Rev. D **25**, 746 (1982).

[21] T.S. Biro, E. van Doorn, B. Müller, M.H. Thoma, and X.-N. Wang, Phys. Rev. C **48**, 1275 (1993).

[22] K.J. Eskola, K. Kajantie, and J. Lindfors, Nucl. Phys. B **323**, 37 (1989).

[23] X.N. Wang and M. Gyulassy, Phys. Rev. D **44**, 3501 (1991).

[24] L.D. McLerran and R. Venugopalan, Phys. Rev. D **49**, 2233 (1994); *ibid.* **49**, 3352 (1994).

[25] J. Adams et al (STAR Collaboration), Phys. Rev. C **70**, 054907 (2004).

[26] P. Arnold, J. Lenaghan, G.D. Moore and L.G. Yaffe, Phys. Rev. Lett. **94**, 072302 (2005).

[27] A. Rebhan, P. Romatschke, and M. Strickland, Phys. Rev. Lett. **94**, 102303 (2005).

[28] A. Dumitru and Y. Nara, Phys. Lett. B **621**, 89-95 (2005).

[29] S. Mrowczynski, Acta. Phys. Polon. B **37**, 427-454 (2006).

[30] J.D. Bjorken, Phys. Rev. D **27**, 140 (1983).